Petteri Parkkila

Fluorescence Correlation Spectroscopy: Theory and Application to Langmuir Monolayers

School of Electrical Engineering

Thesis submitted for examination for the degree of Master of Science in Technology.

Espoo 20.5.2015

Thesis supervisor:

Prof. Paavo Kinnunen

Thesis advisor:

Prof. Jukka Tulkki

Aalto University
School of Electrical
Engineering

AALTO UNIVERSITY
SCHOOL OF ELECTRICAL ENGINEERING

ABSTRACT OF THE
MASTER'S THESIS

Author: Petteri Parkkila

Title: Fluorescence Correlation Spectroscopy: Theory and Application to Langmuir Monolayers

Date: 20.5.2015 Language: English Number of pages: 9+55

Department of Neuroscience and Biomedical Engineering

Professorship: Biophysics and Biomedical Engineering Code: Tfy-99

Supervisor: Prof. Paavo Kinnunen

Advisor: Prof. Jukka Tulkki

Fluorescence correlation spectroscopy (FCS) is a powerful statistical method, which utilizes an autocorrelation analysis of fluorescence intensity fluctuations. Fitting the analytic autocorrelation function to the experimental correlation data makes it possible to quantify time-scales of relevant biophysical properties, such as translational diffusion, triplet state blinking, and chemical reactions. The first part of the thesis presents the fundamental theoretical aspects relevant to the FCS analysis, beginning with the propagation of laser light in a confocal system. Aspects of fluorescence radiation, confocal microscopy, and autocorrelation analysis are examined in a systematic manner. The final chapter of the theoretical part introduces Langmuir monolayers, which are the model membranes of choice for the biophysical experiments concerning oxidative stress.

The oxidatively modified lipids influence important membrane properties and functions. In the second part of the thesis, pressure-dependent diffusion times of fluorophore-probed lipids are investigated in Langmuir monolayers consisting of 1-palmitoyl-2-oleoyl-*sn*-glycerol-3-phosphocholine (POPC), sphingomyelin (SM), cholesterol (Chol) and oxidatively truncated phospholipids. The measurements using FCS and wide-field microscopy combined with a custom-built Langmuir monolayer trough quantitatively confirm that oxidative phosphatidylcholines prevent the disintegration of the SM/Chol-enriched lipid domains. To the author's knowledge, these are the first FCS results on miscibility transition in "raft mixture" lipid monolayers, verifying the previous results obtained using Brewster angle microscopy on such lipid monolayers.

Keywords: fluorescence correlation spectroscopy, confocal microscopy, Langmuir monolayers, oxidative stress

AALTO-YLIOPISTO
SÄHKÖTEKNIIKAN KORKEAKOULU

DIPLOMITYÖN
TIIVISTELMÄ

Tekijä: Petteri Parkkila

Työn nimi: Fluoresenssikorrelaatiospektroskopian teoria ja soveltaminen Langmuir-lipidikalvoihin

Päivämäärä: 20.5.2015 Kieli: Englanti Sivumäärä: 9+55

Neurotieteen ja lääketieteellisen tekniikan laitos

Professuuri: Biofysiikka ja lääketieteellinen tekniikka Koodi: Tfy-99

Valvoja: Prof. Paavo Kinnunen

Ohjaaja: Prof. Jukka Tulkki

Fluoresenssikorrelaatiospektroskopia on tehokas tilastolliseen analyysiin pohjautuva tutkimusmenetelmä, joka perustuu fluoresenssivalon ajallisen vaihtelun tutkimiseen autokorrelaation avulla. Analyyttisen autokorrelaatiofunktion sovittaminen kokeelliseen korrelaatiodataan mahdollistaa erilaisten biofysikaalisten prosessien, kuten diffuusion, triplettisiirtymisten sekä kemiallisten reaktioiden aikaskaalojen määrittämisen. Diplomityön ensimmäinen osa käsittelee fluoresenssikorrelaatiospektroskopian teoriaa lähtien laservalon etenemisestä optisessa systeemissä. Tämän jälkeen käydään systemaattisesti läpi fluoresenssi-ilmiön, konfokaalimikroskopian sekä autokorrelaatioanalyysin perusperiaatteet. Lopuksi perehdytään Langmuir-lipidikalvoihin, jotka toimivat solukalvomalleina työn kokeellisessa osiossa.

Lipidien hapettumisen on tutkimuksissa todettu vaikuttavan solukalvojen rakenteeseen ja toiminnallisuuteen. Diplomityön toisessa osassa 1-palmitoyyli-2-oleoyyli-*sn*-glyseroli-3-fosfatidyylikoliinista (POPC), sfingomyeliinistä (SM) ja kolesterolista (Chol) koostuvien yksikerroksisten Langmuir-lipidikalvojen diffuusio-ominaisuuksia tutkittiin hapettuneiden lipidien läsnäollessa. Fluoresenssikorrelaatiospekroskopian sekä fluoresenssimikroskopian avulla voidaan kvantitatiivisesti näyttää, että hapettuneet fosfolipidit pitkittävät sfingomyeliinistä ja kolesterolista koostuvien järjestyneiden alueiden hajoamista kalvon paineen kasvaessa. Tämä vahvistaa aikaisemmat Brewsterin kulmien analyysiin perustuvalla mikroskopialla saadut tulokset.

Avainsanat: fluoresenssikorrelaatiospektroskopia, konfokaalimikroskopia, lipidien hapettuminen, Langmuir-lipidikalvot

Preface

The experimental work in this Master's Thesis was done while the author was working at the Helsinki Biophysics and Biomembrane Group (HBBG) in the Department of Neuroscience and Biomedical Engineering (former Department of Biomedical Engineering and Computational Science) at Aalto University. The work was carried out in collaboration with the Hof Fluorescence Group in Biophysical Chemistry Department at the Jaroslav Heyrovsky Institute of Physical Chemistry, Academy of Sciences of the Czech Republic (ASCR). The work has been supported by a travel grant from European Science Foundation (EuroMEMBRANE).

I want to thank Professor Jukka Tulkki for taking the arduous task of reviewing my thesis. I express my gratitude to Professor Paavo Kinnunen for all the opportunities and knowledge I have gained at HBBG, and Professor Martin Hof for his extensive guidance and hospitality during my month-long visit to his laboratory in October 2012. I also want to thank my colleagues PhDs Vladimir Zamotin and Roberto Tejera-Garcia at HBBG who introduced me to science, and truly treated me as an equal despite me being just at the start of my career. Last but not least, I am much obliged to PhDs Martin Štefl and Agnieszka Olżyńska for assisting me in Prague and for all their enthusiastic work with our publication.

Above all, thanks to my parents for always being in my support during good and hard times. Thank you, my fellow singers in the Polytech Choir and all other people I have met during my studies.

Otaniemi, 20.5.2015

Petteri Parkkila

Contents

Abstract ii
Abstract (in Finnish) iii
Preface iv
Contents v
Symbols and abbreviations vii

1 Introduction **1**

I Theory **4**

2 Laser beam propagation **5**
2.1 Angular spectrum representation 5
2.2 Paraxial approximation 7
2.3 Far-fields 8
2.4 Focused beams 9
2.5 Airy pattern 13
2.6 Lorentzian and Gaussian approximations 13
2.7 Peak intensity and average power 14

3 Fluorescence phenomenon **16**
3.1 Fluorescence 16
3.2 Absorption rate 18
3.3 Rate equations 19
3.4 Steady-state analysis 20

4 Confocal microscopy **22**
4.1 Confocal principle 22
4.2 Dipolar source in image space 22
4.3 Point spread function 25

5 Fluorescence Correlation Spectroscopy **27**
5.1 Derivation of the autocorrelation function 27
5.2 Diffusion equation 29
5.3 Rotational diffusion 29
5.4 Translational diffusion 30
5.5 Triplet kinetics 31

5.6 Analytic form of the autocorrelation function 33
5.7 Numerical calculations 34

6 Langmuir monolayers **37**

II Experiments **39**

7 Materials and methods **40**
7.1 Sample preparation 40
7.2 Measurements 40

8 Results **43**
8.1 Oxidized phospholipids in POPC monolayers 43
8.2 Oxidized phospholipids in a ternary "raft mixture" 43

9 Summary and conclusions **48**

References **50**

Symbols and abbreviations

Symbols

$\mathbf{E}$	electric field strength
$\mathbf{B}$	magnetic flux density
ϵ	permittivity of the medium / molar extinction coefficient
μ	permeability of the medium / magnitude of the transition dipole moment vector
$\widetilde{\mathbf{A}}$	complex vector field
$\mathbf{k}$	wave vector
ω	angular frequency
c	speed of light in vacuum ($\approx 3 \times 10^8$ m/s) / sample concentration
n	index of refraction
λ	wavelength / eigenvalues of the rate matrix
$\hat{\mathbf{A}}$	Fourier transform of a vector field
$\hat{H}$	optical transfer function
$\mathbf{E}_0$	amplitude vector of linearly polarized electric field
w, w_0	effective beam radius, beam waist radius
z_0	Rayleigh range
R	wavefront radius
η	phase correction factor
$\widetilde{\mathbf{E}}_\infty$	electric farfield
NA	numerical aperture
θ_{max}	maximum half-angle of the focused beam
f	focal length
$\mathbf{E}_{inc}$	paraxial incident electric field
t^s, t^p	Fresnel transmission coefficients
f_0	filling factor
f_a	apodization function
$\mathbf{H}$	magnetic field strength
u, v	optical units
$\mathbf{S}$	Poynting vector
$\Delta r_\parallel$	Airy disk radius
Δz	depth of field
I	intensity (irradiance)
P	power
Q	photon yield
$k_{\alpha\beta}$	transition decay rate from state α to β
k_r, k_{nr}	radiative and non-radiative decay rates
τ_f, τ_T	fluorescence and triplet state lifetimes
$\boldsymbol{\mu}$	transition dipole moment vector
$\overleftrightarrow{\alpha}$	tensorial polarizability
σ	absorption cross-section / variance
N_A	Avogadro constant ($\approx 6.022 \times 10^{23}$ mol^{-1})

$\hbar$	Planck constant ($\approx 1.055 \times 10^{-34}$ m^2 kg/s)
$\mathbf{K}$	transition rate matrix
$\mathbf{P}$	probability matrix
Π	state of the molecule / surface pressure
$P_{\alpha,\beta}$	transition probability from state α to β, i.e. the entries of the probability matrix
S_0, S_1, T	population occupancies of singlet and triplet states
$\overline{A}$	steady state value of A
F	fluorescence intensity
$\overleftrightarrow{\mathbf{G}}_{PSF}$	Green's dyadic point spread function
$\boldsymbol{\mu}$	transition dipole moment vector
M	transverse objective magnification / number of states
Ω	Detector point spread function
Θ	Molecular detection function (MDF)
N	number of molecules
$\langle A \rangle_t$	temporal average of A
G	fluorescence autocorrelation function
g	fluorescence fluctuation autocorrelation function
p	probability density function
$\langle A \rangle$	ensemble average of A
D_T, D_R	translational and rotational diffusion coefficients
∇	gradient operator of space
L	angular momentum operator
τ_D	diffusion time
A	area
γ	surface tension / overlapping factor
a	molecular area

Abbreviations

AOM	acusto-optical modulator
AOTF	acusto-optical tunable filter
BSA	bovine serum albumin
CCD	Charge-Coupled Device
CEF	collection efficiency function
Chol	cholesterol
FCS	fluorescence correlation spectroscopy
FRET	Förster resonance energy transfer
HOMO	highest occupied molecular orbital
LC	liquid-condensed phase
LE	liquid-expanded phase
L_d	liquid-disordered phase
L_o	liquid-ordered phase
LUMO	lowest unoccupied molecular orbital
MDF	molecular detection function
oxPL	oxidized phospholipids
OTF	optical transfer function
PazePC	1-palmitoyl-2-azelaoyl-*sn*-glycero-3-phosphocholine
POPC	1-palmitoyl-2-oleoyl-*sn*-glycerol-3-phosphocholine
POPE	1-palmitoyl-2-oleoyl-*sn*-glycero-3-phosphoethanolamine
PoxnoPC	1-palmitoyl-2-(9'-oxononanoyl)-*sn*-glycero-3-phosphocholine
PSF	point spread function
SM	sphingomyelin
SPAD	single-photon avalanche diode
TEM	transverse electromagnetic mode
WFM	wide-field fluorescence microscopy

Chapter 1

Introduction

Since the development of the light microscopy and the ability to image living cells, scientists have craved to reach beneath the cellular level, in the hopes of understanding various processes essential to life. These ambitions have been suppressed by the inescapable resolution limits of optical microscopes. Consequently, physicists have tried to bypass these limits by asking: what if we could measure a signal coming from the ensemble of molecules we are not able to image, and deduce some biologically relevant physical quantities from that signal. In fact, this is the essence of *fluorescence correlation spectroscopy* (FCS). In FCS, a sample of fluorescent molecules is illuminated with a narrow beam of laser light. When the concentration of molecules in the sample is very low, the emission signal can arise from just one molecule at a time, and in that sense, FCS can be regarded as a single molecule technique.

Despite that FCS originated mainly from the experimental needs, concepts in theoretical physics developed in mid-1950s greatly aided its evolution. In 1972, Elson, Magde and Webb laid the foundations of FCS by describing how the chemical kinetics of fluorescent molecules, coupled with translational diffusion, can be studied in the sample illuminated by a Gaussian laser beam [1]. Their research was largely influenced by the work of Berne and Pecora on dynamic light scattering just a few years earlier [2]. The research of Elson *et al.* gave the general term to the correlation-based analysis of the fluorescence time traces, *fluctuation correlation spectroscopy*. Fluctuations of the concentration of the fluorescent complex around the equilibrium value, in their setup, induced a photocurrent in the detector located in the vicinity of the sample. An important outcome was the concept of autocorrelation. By studying the self-similarity of the recorded signal as a function of time-lag, one can quantify the characteristic times for many biologically relevant processes, not just diffusion or chemical kinetics. Indeed, Aragon and Pecora did their pioneering work in 1975 by calculating correlation functions for rotational diffusion [3, 4]. For the following decades, FCS raised merely academic interest. Eventually, interest in the FCS was revived upon the availability of sufficient computational power to analyze the recorded fluorescence signals in real-time. Since then, FCS has been improved to cover novel techniques such as cross-correlation spectroscopy (FCCS), 2-focus FCS, intracellular measurements and even molecular imaging [5–8].

Figure 1.1 demonstrates the basic principle behind FCS. A confocal microscopy setup is utilized to focus laser light through an objective with high numerical aperture into a

Figure 1.1: Molecules diffusing through the detection volume generates fluorescence fluctuations due to the various physical processes.

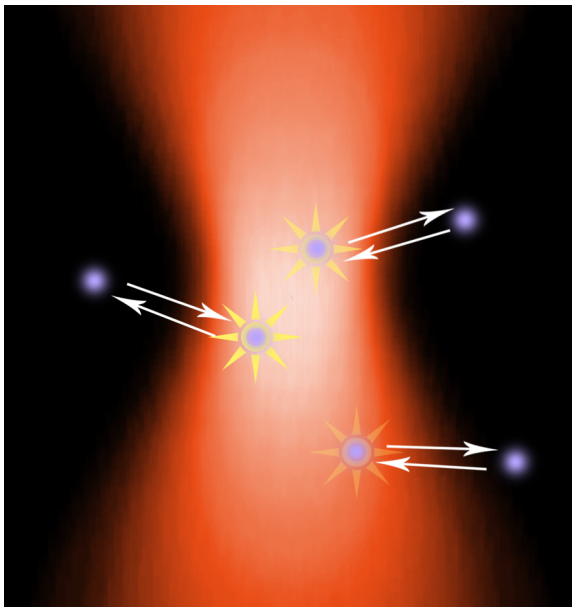

small detection volume ($\sim$ 1 fl). Fluorescent molecules wander through this focus, eventually emitting fluorescence radiation with different intensities depending on the distance from the beam center. During its time in the focus, a molecule may experience chemical conversion, bind to a macromolecule, or be repelled by membrane raft structures, for instance. All these changes affect the radiation the molecule emits. The pinhole of the confocal microscope system effectively blocks any excess radiation coming far away from the focus. Detector behind the pinhole transforms the energy of the photon flux to photocurrent signal, which in turn can be digitalized with modern electronics. In addition to the experimental setup, FCS has special requirements for fluorescent dyes. A fluorophore should not only have high photon yield and large absorption cross section, but also high photostability in order to withstand enormous laser intensity in the focus [9].

Part I of the thesis aims to cover the theoretical aspects of FCS adequately, starting from the propagation of laser radiation in modern optical systems. Then the fluorescence phenomenon is explored as an analogue to a simple chemical reaction scheme with multiple energy states. Confocal microscopy, an essential part of a modern FCS setup, is briefly discussed along with the properties of dipole radiation and the effect of a pinhole on the fluorescence detection efficiency. Autocorrelation analysis, which serves as a statistical tool for retrieving the desired parameters from an experiment, is treated with specific formalism. The theoretical part is finished with an introduction to Langmuir monolayers, building a necessary bridge to the experimental part of the thesis. There is a whole book written about FCS, which tells something about the vastness of the subject [10]. Therefore, themes not crucial for understanding FCS or the experiments are not covered.

Figure 1.2: Chemical structures of two oxidatively truncated phosphatidylcholines, PazePC and PoxnoPC.

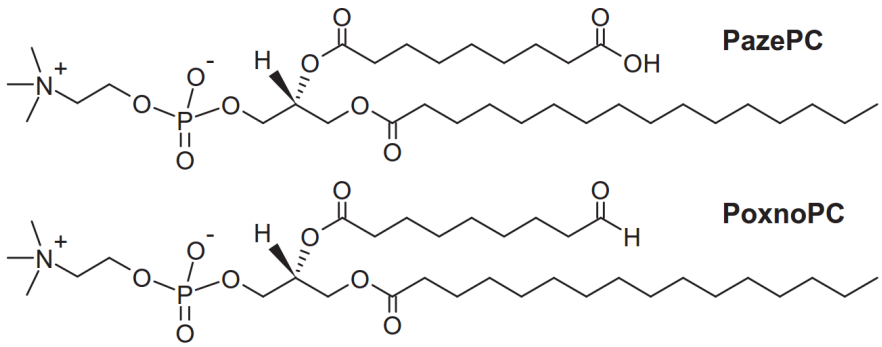

Oxidative stress is known to have an impact on cell membrane properties such as modulation of signaling complexes and lipid-protein interactions. Recent advancements in cell biology point to the involvement of oxidized lipids in processes such as molecular pathology, apoptosis, and inflammation [11–13]. For example, it was found that the addition of oxidized phosphatidylcholines into 1-palmitoyl-2-oleoyl-*sn*-glycerol-3-phosphocholine (POPC) bilayers abrupts the permeability barrier function of the bilayer. The rapid loss of lipid asymmetry in turn facilitates phospholipid flip-flop during apoptosis [14]. In conclusion, the detailed understanding of lipid biophysics will aid the analysis of cell behavior, which has traditionally been explained mainly by protein functionality.

It has been shown by using Brewster angle methods that the lipid oxidation effectually promotes the domain separation in POPC, sphingomyelin (SM) and cholesterol (Chol)-enriched Langmuir monolayers. Brewster angle microscopy demonstrated oxidatively truncated phosphatidylcholines to promote phase separation in Langmuir monolayers consisting of POPC, sphingomyelin (SM) and cholesterol (Chol) [15]. More specifically, 1-palmitoyl-2-azelaoyl-*sn*-glycero-3-phosphocholine (PazePC), was found to increase the miscibility transition pressure of the liquid-ordered (L_o) SM/Chol-domains. The aim of the experiments (Part II) was to investigate the diffusional dynamics of these monolayers using FCS and wide-field imaging. After incorporating two oxidatively truncated phosphatidylcholines (Fig. 1.2), PazePC and PoxnoPC (1-palmitoyl-2-(9'-oxononanoyl)-*sn*-glycero-3-phosphocholine) to the liquid-disordered (L_d) phase of the ternary "raft" monolayers, the resulting changes in diffusion times as a function of monolayer surface pressure were analyzed using theoretical models described in Part I. Experimental results represented in the thesis have been published in *Biochimica et Biophysica Acta (BBA)* [16].

Part I

Theory

Chapter 2

Laser beam propagation

To understand any method based on optical microscopy, one has to examine how a laser beam propagates through the optical system. In this section, the fundamental properties of propagating laser beams are derived starting from Maxwell equations. First, laser beams are studied in the limit of paraxial approximation with a low degree of beam divergence. Then the beam behavior is inspected far away from the source. Finally, these results are combined with the theory of strongly focused Gaussian laser beams involving an aplanatic lens that represents the microscope objective in a confocal system. The calculated diffraction-based formulas are then approximated with Gaussian and Lorentzian profiles relevant to the FCS analysis.

2.1 Angular spectrum representation

In linear, homogenous and non-dispersive medium in absence of free charges or currents, Maxwell's equations for electric field strength $\mathbf{E}$ and magnetic flux density $\mathbf{B}$ read

$$\nabla \cdot \mathbf{E} = 0, \tag{2.1}$$

$$\nabla \times \mathbf{E} = -\frac{\partial \mathbf{B}}{\partial t}, \tag{2.2}$$

$$\nabla \cdot \mathbf{B} = 0, \tag{2.3}$$

$$\nabla \times \mathbf{B} = \mu\epsilon \frac{\partial \mathbf{E}}{\partial t}, \tag{2.4}$$

where ϵ is permittivity and μ is permeability of the medium. Also, the medium is assumed as lossless (perfect dielectric), and therefore $\Im\mathrm{m}(\epsilon) = 0$. By using the vector identity

$$\nabla \times (\nabla \times \mathbf{A}) = \nabla (\nabla \cdot \mathbf{A}) - \nabla^2 \mathbf{A} \tag{2.5}$$

and taking the curl of equation (2.2),

$$\nabla \times (\nabla \times \mathbf{E}) = \nabla (\nabla \cdot \mathbf{E}) - \nabla^2 \mathbf{E} = -\nabla^2 \mathbf{E} \tag{2.6}$$

for the left-hand side and

$$\nabla \times \left(-\frac{\partial \mathbf{B}}{\partial t} \right) = -\frac{\partial}{\partial t} (\nabla \times \mathbf{B}) = -\mu\epsilon \frac{\partial^2 \mathbf{E}}{\partial t^2} \tag{2.7}$$

for the right-hand side yields

$$\nabla^2 \mathbf{E} = \mu\epsilon \frac{\partial^2 \mathbf{E}}{\partial t^2}, \tag{2.8}$$

which is the wave equation for electric field. A set of solutions to the wave equation is the set of complex plane waves of the form

$$\widetilde{\mathbf{E}}(\mathbf{r}, t) = \mathbf{E}(\mathbf{r}) e^{i(\mathbf{k}\cdot\mathbf{r} - \omega t)} = \widetilde{\mathbf{E}}(\mathbf{r}) e^{-i\omega t}, \tag{2.9}$$

where the propagation and position vectors are given by $\mathbf{k} = k_x\hat{x} + k_y\hat{y} + k_z\hat{z}$ and $\mathbf{r} = x\hat{x} + y\hat{y} + z\hat{z}$. It is important to stress that $\widetilde{\mathbf{E}}(\mathbf{r})$ represents complex amplitude of a wave propagating with the angular frequency of ω. The wave vector $\mathbf{k}$ has magnitude of

$$|\mathbf{k}| = k = \omega\sqrt{\mu\epsilon} = \frac{\omega n}{c} = \frac{2\pi n}{\lambda}, \tag{2.10}$$

where n is the (constant) index of refraction in pure dielectric medium c is the speed of light in vacuum and λ is the wavelength. Thus, substitution of complex wave function (2.9) to the wave equation yields the Helmholtz equation

$$(\nabla^2 + k^2)\widetilde{\mathbf{E}}(\mathbf{r}) = 0. \tag{2.11}$$

Since the field is time-harmonic, term $e^{-i\omega t}$ can be omitted. Helmholtz equation is a partial differential equation of the second order having infinite number of solutions. Particularly, Helmholtz equation gives the solutions or modes for electromagnetic radiation emerging from a laser cavity. However, lasers used in typical optical systems operate in the *transverse electromagnetic mode* of the lowest order (TEM_{00}) and thus only the fundamental Gaussian solution is needed. The solution in all transverse planes can be obtained by Fourier analysis. The two-dimensional Fourier transform of the complex field $\widetilde{\mathbf{E}}(x, y, z)$ is defined as

$$\mathcal{F}\{\widetilde{\mathbf{E}}(x, y, z)\} = \hat{\mathbf{E}}(k_x, k_y;\, z) = \frac{1}{4\pi^2} \iint_{-\infty}^{\infty} \widetilde{\mathbf{E}}(x, y, z) e^{-i(k_x x + k_y y)}\, \mathrm{d}x\mathrm{d}y, \tag{2.12}$$

where k_x, k_y are the spatial frequencies corresponding to the Cartesian transverse coordinates x, y. The inverse Fourier transform gives the original field as

$$\mathcal{F}^{-1}\{\hat{\mathbf{E}}(k_x, k_y;\, z)\} = \widetilde{\mathbf{E}}(x, y, z) = \iint_{-\infty}^{\infty} \hat{\mathbf{E}}(k_x, k_y;\, z) e^{i(k_x x + k_y y)}\, \mathrm{d}k_x\mathrm{d}k_y. \tag{2.13}$$

Fourier transforming the Helmholtz equation and recalling that $\widetilde{\mathbf{E}}(x, y, z) = \widetilde{\mathbf{E}}(x, y, 0)$ $e^{ik_z z}$ gives

$$\hat{\mathbf{E}}(k_x, k_y;\, z) = \hat{\mathbf{E}}(k_x, k_y;\, 0) e^{ik_z z} = \hat{\mathbf{E}}(k_x, k_y;\, 0)\hat{H}(k_x, k_y;\, z), \tag{2.14}$$

where $e^{ik_z z} = \hat{H}(k_x, k_y; z)$ is a propagator or optical transfer function (OTF) describing the modification of the angular spectrum along the positive z-axis. Fourier spectrum in the object plane can be written as

$$\hat{\mathbf{E}}(k_x, k_y;\, 0) = \frac{1}{4\pi^2} \iint_{-\infty}^{\infty} \widetilde{\mathbf{E}}(x', y';\, 0) e^{-i(k_x x' + k_y y')}\, \mathrm{d}x'\mathrm{d}y'. \tag{2.15}$$

Substitution of equations (2.14) and (2.15) to the inverse Fourier transform representation (2.13) gives

$$\widetilde{\mathbf{E}}(x,y,z) = \frac{1}{4\pi^2}\iint_{-\infty}^{\infty}\widetilde{\mathbf{E}}(x',y';\,0)\iint_{-\infty}^{\infty}\mathrm{e}^{i[k_x(x-x')+k_y(y-y')+k_z z]}\,\mathrm{d}x'\mathrm{d}y'\mathrm{d}k_x\mathrm{d}k_y, \tag{2.16}$$

which is the *angular spectrum representation* of electromagnetic radiation travelling to the direction of positive z-axis.

The importance of the wave vector $\mathbf{k} = (k_x, k_y, k_z)$ in defining the solutions has not yet been discussed. If the component $k_z = \sqrt{k^2 - k_x^2 - k_y^2}$ is real so that $k_x^2 + k_y^2 \leq k^2$, the resulting waves are plane waves. On the other hand, for $k_x^2 + k_y^2 > k^2$, *evanescent waves* are encountered. For example, if $k_x^2 + k_y^2 = \alpha k^2$ where $\alpha > 1$, the propagator $\mathrm{e}^{ik_z z}$ becomes

$$\mathrm{e}^{ik_z z} = \mathrm{e}^{(1-\alpha)kz}, \tag{2.17}$$

which is an exponentially decaying function. Higher the α, higher spatial oscillations are achieved but also stronger the field decay along the z-axis will be.

2.2 Paraxial approximation

In the previous section, the angular spectrum representation for plane wave solutions of Helmholtz equation was derived. An important outcome was that the knowledge of electric field distribution in an arbitrary (image) plane $z' = 0$ gives a way to calculate the fields in all transverse (object) planes via inverse Fourier transform. However, a problem arises from the wave vector $\mathbf{k}$ when solving the angular spectrum representation analytically. Laser beam propagation has characteristics of both plane and spherical waves; thus the spatial contributions to the wave vector become more significant far from the beam center $(x, y, z) = (0, 0, z)$. Fortunately, for Gaussian laser beams, these spatial contributions can be considered small so that $k_x^2 + k_y^2 \ll k$. Taylor expansion of k_z gives

$$k_z = k\sqrt{1 - \frac{k_x^2 + k_y^2}{k^2}} \approx k - \frac{k_x^2 + k_y^2}{2k}. \tag{2.18}$$

Of course, this requires that the half-angle of beam divergence θ is small. The result is called *paraxial approximation*.

Assuming a fundamental laser beam with linearly polarized field distribution, the electric field in the laser beam waist has a form

$$\mathbf{E}(x',y';\,0) = \mathbf{E}_0\,\mathrm{e}^{-\frac{x'^2+y'^2}{w_0^2}}, \tag{2.19}$$

where $\mathbf{E}_0$ is a constant field vector in transverse object plane (x', y') at $z' = 0$. For instance, linearly polarized radiation has $\mathbf{E}_0 = E_0\,\hat{x}$ if the field is polarized in the x-direction. *Beam*

waist radius w_0 corresponds to the radius where the electric field vector has attenuated to the value of $(1/\mathrm{e})E_0$. Fourier spectrum can be calculated as

$$\begin{aligned}\hat{\mathbf{E}}(k_x, k_y;\, 0) &= \frac{1}{4\pi^2}\iint_{-\infty}^{\infty}\mathbf{E}_0\,\mathrm{e}^{-\frac{x'^2+y'^2}{w_0^2}}\,\mathrm{e}^{-i(k_x x'+k_y y')}\,\mathrm{d}x'\mathrm{d}y' \\ &= \mathbf{E}_0\frac{w_0^2}{4\pi}\,\mathrm{e}^{-(k_x^2+k_y^2)\frac{w_0^2}{4}}.\end{aligned} \tag{2.20}$$

Replacing k_z with paraxial expression from (2.18) and integrating angular spectrum representation gives

$$\begin{aligned}\widetilde{\mathbf{E}}(x, y, z) &= \mathbf{E}_0\frac{w_0^2}{4\pi}\,\mathrm{e}^{ikz}\iint_{-\infty}^{\infty}\mathrm{e}^{-(k_x^2+k_y^2)(\frac{w_0^2}{4}+\frac{iz}{2k}}\,\mathrm{e}^{i(k_x x+k_y y)}\,\mathrm{d}x'\mathrm{d}y' \\ &= \frac{\mathbf{E}_0\,\mathrm{e}^{ikz}}{1+2iz/kw_0^2}\,\mathrm{e}^{-\frac{x^2+y^2}{w_0^2}\frac{1}{1+2iz/kw_0^2}}.\end{aligned} \tag{2.21}$$

Usually the equation is written by defining parameters $\rho^2 = x^2 + y^2$ and $z_0 = kw_0^2/2$, which is the *Rayleigh range*. This gives the paraxial Gaussian beam representation

$$\widetilde{\mathbf{E}} = \mathbf{E}_0\frac{w_0}{w(z)}\,\mathrm{e}^{-\frac{\rho^2}{w(z)^2}}\,\mathrm{e}^{i[kz-\eta(z)+k\rho^2/2R(z)]} \tag{2.22}$$

with the abbreviations [17, p. 48]

$$\begin{aligned} w(z) &= w_0\sqrt{1+\frac{z^2}{z_0^2}} && \textit{beam waist radius}, \\ R(z) &= z\left(1+\frac{z_0^2}{z^2}\right) && \textit{wavefront radius}, \\ \eta(z) &= \tan^{-1}\frac{z}{z_0}. && \textit{phase correction}. \end{aligned} \tag{2.23}$$

2.3 Far-fields

In order to calculate the electric field at the far field points $\mathbf{r} = \mathbf{r}_\infty$, the unit vector $\hat{s}$ is introduced as

$$\hat{s} = (s_x, s_y, s_z) = (x, y, z)\frac{1}{r}, \tag{2.24}$$

where r is the distance of field point $\mathbf{r}_\infty$ from the origin. Therefore, the angular spectrum representation reads

$$\widetilde{\mathbf{E}}_\infty(s_x, s_y, s_z) = \lim_{kr\to\infty}\iint_{k_x^2+k_y^2\le k^2}\hat{\mathbf{E}}(k_x, k_y;\, 0)\mathrm{e}^{ir(k_x s_x+k_y s_y+k_z s_z)}\,\mathrm{d}k_x\mathrm{d}k_y \tag{2.25}$$

with the integration limited to the region with no decaying evanescent waves, as their contribution is negligible in the limit $kr \to \infty$. The integral can be calculated by the method of stationary phase, giving

$$\widetilde{\mathbf{E}}_\infty(s_x, s_y, s_z) = -2\pi i k s_z \hat{\mathbf{E}}(k s_x, k s_y; 0)\frac{\mathrm{e}^{ikr}}{r}, \tag{2.26}$$

where e^{ikr}/r follows from the *aplanatic approximation*. In this approximation, the principal radii of curvature of the far-field wavefront $\sqrt{R_1 R_2}$ and eikonal function have the same value, r [18]. The far-fields are defined by the object plane Fourier fields $\hat{\mathbf{E}}(k_x, k_y; 0)$ with the substitution $k_x \to k s_x$ and $k_y \to k s_y$. This also means that

$$\hat{s} = (s_x, s_y, s_z) = (k_x, k_y, k_z)\frac{1}{k}, \tag{2.27}$$

implying that one plane wave of the Fourier spectrum at $z = 0$ contributes to the far-field in the direction $\hat{s}$. Expressing the Fourier spectrum of the object plane in terms of far-field gives

$$\hat{\mathbf{E}}(k_x, k_y; 0) = \frac{ir\mathrm{e}^{-ikr}}{2\pi k_z}\widetilde{\mathbf{E}}_\infty(k_x, k_y) \tag{2.28}$$

Finally, the angular spectrum representation can be written in terms of far-field as

$$\widetilde{\mathbf{E}}(x, y, z) = \frac{ir\mathrm{e}^{-ikr}}{2\pi}\iint\limits_{k_x^2+k_y^2\le k^2} \widetilde{\mathbf{E}}_\infty(k_x, k_y)\mathrm{e}^{i(k_x x + k_y y + k_z z)}\frac{1}{k_z}\,\mathrm{d}k_x\mathrm{d}k_y. \tag{2.29}$$

This result has importance when deriving the field for focused beams in the next section.

2.4 Focused beams

In confocal microscopy, the laser beam is focused to the sample with an objective with high numerical aperture. For instance, a water immersion ($n = 1.33$) objective with $NA = n\sin\theta_{max} = 1.2$ gives a maximum half-angle of $\theta_{max} = 64.2°$. Then the relative error for the longitudinal wave component k_z is

$$\frac{\Delta k_z}{k_z} = \frac{1 - \frac{k_x^2+k_y^2}{2k^2}}{\sqrt{1 - \frac{k_x^2+k_y^2}{k^2}}} - 1 = \frac{1 - \frac{1}{2}\sin^2\theta_{max}}{\sqrt{1 - \sin^2\theta_{max}}} - 1 \approx 36,5\%. \tag{2.30}$$

Therefore, the paraxial approximation is no longer valid after strong beam focusing.

Beam focusing is achieved by passing a paraxial optical field $\mathbf{E}_{inc}$ through an aplanatic optical lens with focal length f (Fig. 2.1). In the mathematical treatment, it is denoted that the lens is treated as a reference sphere transforming the incident rays from cylindrical coordinates (ρ, ϕ, z) to spherical coordinates (r, ϕ, θ). The reference sphere $r = f$ is considered as a far field surface $(x_\infty, y_\infty, z_\infty)$ with total refracted electric field

$$\widetilde{\mathbf{E}}_\infty = \widetilde{\mathbf{E}}_{inc}\sqrt{\frac{\cos\theta}{n}} \tag{2.31}$$

Figure 2.1: Geometry and coordinates of an aplanatic lens used to derive highly focused field. Illustration is based on Ref. [17, p. 59].

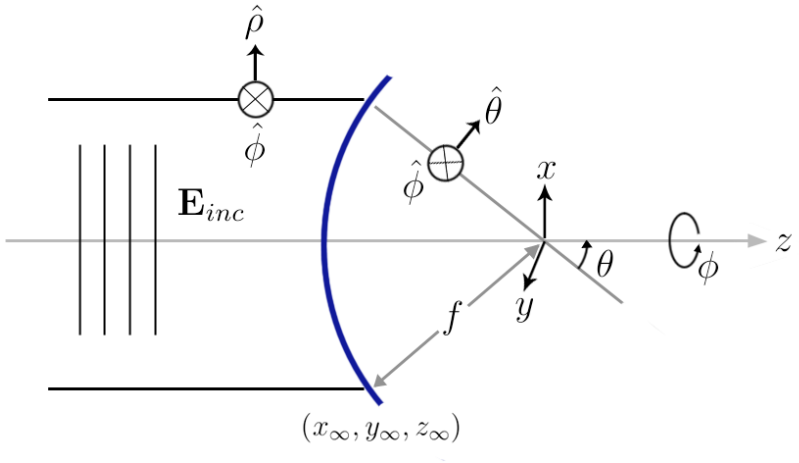

which follows from the conservation of energy. The medium where incoming field propagates has a refractive index of unity and n is the index of the sample medium. Incident field can be divided to the s- and p-polarized parts as

$$\begin{aligned} \widetilde{\mathbf{E}}_{inc}^{(s)} &= [\widetilde{\mathbf{E}}_{inc} \cdot \hat{\phi}]\,\hat{\phi}, \\ \widetilde{\mathbf{E}}_{inc}^{(p)} &= [\widetilde{\mathbf{E}}_{inc} \cdot \hat{\rho}]\,\hat{\rho}. \end{aligned} \tag{2.32}$$

When the two fields refract, the unit vector $\hat{\phi}$ remains the same while the vector $\hat{\rho}$ is mapped into $\hat{\theta}$. Thus, the total refracted field can be written as

$$\widetilde{\mathbf{E}}_{\infty} = \left[t_s[\widetilde{\mathbf{E}}_{inc} \cdot \hat{\phi}]\,\hat{\phi} + [t_p[\widetilde{\mathbf{E}}_{inc} \cdot \hat{\rho}]\,\hat{\theta}\right] \sqrt{\frac{\cos\theta}{n}} \tag{2.33}$$

where t_s and t_p are the Fresnel transmission coefficients for both directions of polarization. Spherical coordinate unit vectors can be expressed in terms of the Cartesian unit vectors as

$$\begin{aligned} \hat{r} &= \cos\phi\,\hat{x} + \sin\phi\,\hat{y}, \\ \hat{\phi} &= -\sin\phi\,\hat{x} + \cos\phi\,\hat{y}, \\ \hat{\theta} &= \cos\theta\cos\phi\,\hat{x} + \cos\theta\sin\phi\,\hat{y} - \sin\theta\,\hat{z}. \end{aligned} \tag{2.34}$$

At this point it is assumed that (i) lens is anti-reflection coated so $t_s = t_p = 1$ and (ii) $\mathbf{E}_{inc}$ is polarized along x-axis so that $\mathbf{E}_{inc} = E_{inc}\,\hat{x}$. This gives

$$\begin{aligned} \mathbf{E}_{\infty}(f;\,\theta,\phi) &= E_{inc}(f;\theta,\phi)(\hat{\theta}\cos\phi - \hat{\phi}\sin\phi)\sqrt{\frac{\cos\theta}{n}} \\ &= E_{inc}(f;\,\theta,\phi)\frac{1}{2}\begin{bmatrix} (1+\cos\theta) - (1-\cos\theta)\cos 2\phi \\ -(1-\cos\theta)\sin 2\phi \\ -2\cos\phi\sin\theta \end{bmatrix}\sqrt{\frac{\cos\theta}{n}}, \end{aligned} \tag{2.35}$$

where the far-field is expressed in Cartesian vector components. However, the incident beam has not yet been defined. It is fair to assume that the incident beam has a Gaussian (0,0) mode beam with amplitude

$$E_{inc} = E_{0,inc}\, \mathrm{e}^{-(x_\infty^2+y_\infty^2)/w_{0,inc}^2} = E_{0,inc}\, \mathrm{e}^{-f^2 \sin^2\theta/w_{0,inc}^2}. \tag{2.36}$$

Defining the *filling factor* f_0 as the ratio of incoming beam waist radius and back-aperture radius,

$$f_0 = \frac{w_{0,inc}}{h} = \frac{w_{0,inc}}{f \sin\theta_{max}}, \tag{2.37}$$

gives a way to write the exponential function in (2.36) as

$$f_a(\theta) = \mathrm{e}^{-\frac{1}{f_0^2}\frac{\sin^2\theta}{\sin^2\theta_{max}}}, \tag{2.38}$$

which is referred as *apodization function* [17, p. 62]. Filling factor tells the degree of over- or underfilling of the beam arriving at the aplanatic lens or objective. Before the insertion of the far-field formula to the angular spectrum representation, the integral coordinate transfer to spherical coordinates is needed. The differentials $\mathrm{d}k_x$ and $\mathrm{d}k_y$ can be transformed as $(1/k_z)\mathrm{d}k_x\mathrm{d}k_y = k\sin\theta\mathrm{d}\phi\mathrm{d}\theta$. In addition, the transverse coordinates (x, y) can be expressed as $x = \rho\cos\varphi$ and $y = \rho\sin\varphi$. Making these substitutions to the (2.29) and noting that $r = f$ yields

$$\widetilde{\mathbf{E}}(\rho,\varphi,z) = \frac{ikf\mathrm{e}^{-ikf}}{2\pi}\int_0^{\theta_{max}}\int_0^{2\pi}\widetilde{\mathbf{E}}_\infty(f;\,\phi,\theta)\mathrm{e}^{ikz\cos\theta}\mathrm{e}^{ik\rho\sin\theta\cos(\phi-\varphi)}\sin\theta\,\mathrm{d}\phi\mathrm{d}\theta. \tag{2.39}$$

The cylindrical coordinate φ is used here to distinguish it from the ϕ representing the spherical coordinates. With the relations

$$\begin{aligned}\int_0^{2\pi}\cos n\phi\,\mathrm{e}^{ix\cos(\phi-\varphi)}\,\mathrm{d}\phi &= 2\pi(i^n)J_n(x)\,\cos n\varphi\\ \int_0^{2\pi}\sin n\phi\,\mathrm{e}^{ix\cos(\phi-\varphi)}\,\mathrm{d}\phi &= 2\pi(i^n)J_n(x)\,\sin n\varphi\end{aligned} \tag{2.40}$$

it is convenient to define single integrals for variable θ as

$$\begin{aligned}W_0 &= \int_0^{\theta_{max}} f_a(\theta)\sin\theta\sqrt{\cos\theta}(1+\cos\theta)J_0(k\rho\sin\theta)\,\mathrm{e}^{ikz\cos\theta}\,\mathrm{d}\theta,\\ W_1 &= \int_0^{\theta_{max}} f_a(\theta)\sin^2\theta\sqrt{\cos\theta}J_1(k\rho\sin\theta)\,\mathrm{e}^{ikz\cos\theta}\,\mathrm{d}\theta,\\ W_2 &= \int_0^{\theta_{max}} f_a(\theta)\sin\theta\sqrt{\cos\theta}(1-\cos\theta)J_2(k\rho\sin\theta)\,\mathrm{e}^{ikz\cos\theta}\,\mathrm{d}\theta,\end{aligned} \tag{2.41}$$

Figure 2.2: Intensity profiles of non-Gaussian (00)-mode laser beams after strong focusing for $NA = 1.2$, $n = 1.33$ and $\lambda = 488$ nm (cyan light). Scaling is presented in optical units, namely $u = kz \sin^2 \theta_{max}$ and $v = k\rho \sin \theta_{max}$.

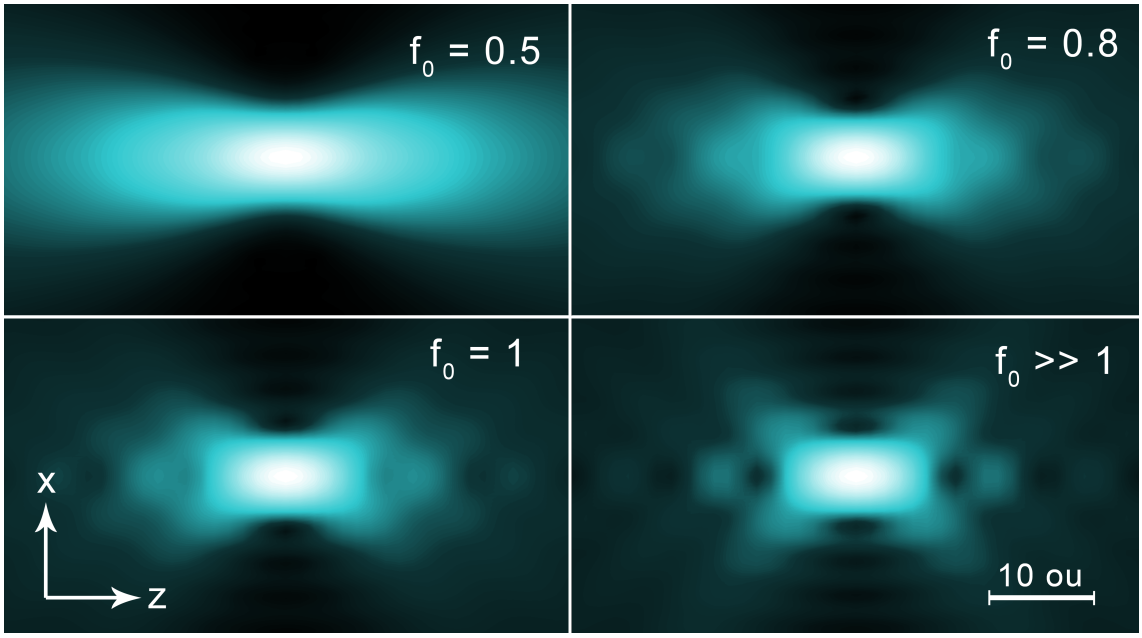

where J_n are the Bessel functions of n-th order. The integrals follow the form of Wolf and Richards except for the apodization function [19]. Finally, using Eq. (2.35) and these abbreviations in Eq. (2.39) yields

$$\widetilde{\mathbf{E}}(\rho, \varphi, z) = iA\, \mathrm{e}^{-ikf} \begin{bmatrix} W_0 + W_2 \cos 2\varphi \\ W_2 \sin 2\varphi \\ -2iW_1 \cos \varphi \end{bmatrix} \tag{2.42}$$

which is the *non-Gaussian field* solution, with $A = kfE_{0_{inc}}/2\sqrt{n}$. The magnetic field strength $\widetilde{\mathbf{H}}$ has similar profile, with the relationship $\mathbf{E} \perp \mathbf{H}$. In practice, the integrals in Eq. (2.41) need to be calculated in each fieldpoint (ρ, z) before insertion. The electric field strength is strongest at the beam waist center $(\rho, z) = (0,0)$ and attenuates in the axial and transverse directions. As shown in the Fig. 2.2, the beam waist radius becomes more narrow under strong over-filling. On the other hand, the shape of the illumination profile approaches Gaussian beam in the limit of low aperture filling. The intensity (irradiance) profile of the laser beam can be easily calculated as

$$\begin{aligned} I(\rho, \varphi, z) = |\langle \mathbf{S} \rangle| &= \frac{1}{2} |\Re\mathrm{e}\{\widetilde{\mathbf{E}} \times \widetilde{\mathbf{H}}^*\}| \\ &= A^2 I_{0,inc} \{|W_0|^2 + |W_2|^2 + 4|W_1|^2 \cos^2 \varphi + 2 \cos 2\varphi\, \Re\mathrm{e}\,(W_0 W_2^*)\}, \end{aligned} \tag{2.43}$$

where $\langle \mathbf{S} \rangle$ is the time-averaged Poynting vector.

2.5 Airy pattern

In the limit of weak beam focusing, θ_{max} is sufficiently low and the approximations $\cos\theta \approx 1$ and $\sin\theta \approx \theta$ are valid. However, the second order approximation, i.e. $\cos\theta \approx 1 - \theta^2/2$, is needed for the cosine function in order to retain the θ-dependence in the integrals of Eq. (2.41). For small arguments, Bessel functions behave as $J_n \approx x^n$. Assuming an over-filled back aperture (with $f_a = 1$), the *paraxial focused field* amplitude can then be written in the focal plane as

$$|\mathbf{E}(\rho, z = 0)| \sim \frac{2J_1(k\rho\theta_{max})}{k\rho\theta_{max}} = \frac{2J_1(v)}{v} \tag{2.44}$$

where $v = k\rho\sin\theta_{max} \approx k\rho\theta_{max}$ are optical units in the radial direction. This function is also called *Airy pattern* due to the fringes existing on the beam edges, and it has significance in regards of the lateral resolution of the confocal system. According to Abbe (1873), the minimum distance from which two point sources can still be distinguished, corresponds to position where maximum of one Airy pattern coincides with the minimum of another. The Abbe resolution limit or *Airy disk radius* is

$$\Delta r_{\parallel} = \frac{3.832}{k\theta_{max}} = \frac{3.832\lambda}{2\pi n\theta_{max}} \approx 0.6098\frac{\lambda}{NA}. \tag{2.45}$$

Microscopists also refer to this quantity as a *resel* [20]. Similarly, in axial direction, paraxial approximation becomes

$$|\mathbf{E}(\rho = 0, z)| \sim \frac{\sin(kz\theta_{max}^2/4)}{kz\theta_{max}^2/4} = \frac{\sin(u/4)}{u/4} \tag{2.46}$$

where $u = kz\sin^2\theta_{max} \approx kz\theta_{max}^2$ are the axial optical units. The distance for which the axial equation becomes zero, is

$$\Delta z = \frac{2n\lambda}{NA^2}, \tag{2.47}$$

which is the *depth of field*. For a water immersion microscope with $\lambda = 488$ nm and $NA = 1.2$, these parameters are $\Delta r_{\parallel} = 248$ nm and $\Delta z = 275$ nm. [18]

2.6 Lorentzian and Gaussian approximations

The Gaussian approximation for paraxial field solution can be found when beam waist radius w_0 is written in terms of divergence half-angle. The solution is then

$$|\mathbf{E}(\rho, z = 0)| \sim \mathrm{e}^{-\frac{\rho^2}{w_0^2}} = \mathrm{e}^{-\frac{\rho^2}{w_0^2}} \tag{2.48}$$

where $w_0 = \lambda/\pi\theta_{max}$ can be written as

$$w_0 = \frac{\lambda}{\pi\sin\theta_{max}} = \frac{n\lambda}{\pi NA}, \tag{2.49}$$

when considering that θ_{max} can be replaced by its sine value [21, p. 86]. If the axial dependence is modelled with the fundamental Gaussian beam of Eq. (2.22), the resulting approximation is called *Lorentzian-Gaussian*. Rayleigh range can be written as

$$z_0 = \frac{kw_0^2}{2} = \frac{\pi n}{\lambda} w_0^2. \tag{2.50}$$

When the axial direction is also approximated with a Gaussian, the laser intensity is purely *Gaussian*, and proportional to

$$I(\rho, z) \sim \mathrm{e}^{-2\left(\rho^2/w_0^2\right)} \mathrm{e}^{-2\left(z^2/w_z^2\right)}, \tag{2.51}$$

where w_z is usually fitted manually to the real profile, but sometimes chosen to be equal to the half-width of the Lorentizan profile, with $w_z = z_0 \sqrt{2/\ln 2}$ [22].

An important outcome of the preceding calculations is that there is now four solutions for focused laser beam fields: non-Gaussian, paraxial, Gaussian-Lorentzian and Gaussian. It is evident that the oscillatory nature of the beam intensity arising from secondary Huygens wavelets from the objective edges cannot be accurately represented by these approximations in the high *NA* limit. Especially with strong over-filling of the beam, approximating the focused beam with simple Gaussian leads to an error when fitting the FCS autocorrelation function to the experimental data. Figure 2.3 shows the three-dimensional shapes of the approximations compared to the non-Gaussian focus with water-immersion objective of $NA = 1.2$. The paraxial approximation is omitted since it is similar to the Gaussian profile, with an elongated axial profile. Approximations are radially symmetric while the non-Gaussian field is protracted in the direction of polarization.

2.7 Peak intensity and average power

So far, only the spatial distribution of light has been discussed. For fluorescence applications, it is important to relate the power given by laser source with the peak intensity of the beam. The intensity of the laser beam has drastic influence on the fluorescence absorption properties of fluorophores passing the beam. Total power P_0 transmitted by the beam could be calculated by integrating time-averaged Poynting vector in any transverse plane since power transmitted is the same in every plane. However, since the distribution of intensity is already known, the peak intensity in the exact beam center, $(\rho, z) = (0, 0)$, is only needed. The peak intensity of highly focused beam is well approximated by the peak intensity of Gaussian beam. For a Gaussian beam, the power transmitted through an aperture with radius ρ at $z = 0$ is

$$P(\rho) = P_0 \left(1 - \mathrm{e}^{-2(\rho/w_0)^2}\right). \tag{2.52}$$

Intensity can be now calculated by dividing the power by the aperture radius, and taking the limit $\rho \to 0$. The L'Hospital rule gives

$$I_0 = \lim_{\rho \to 0} \frac{P_0 \left(1 - \mathrm{e}^{-2(\rho/w_0)^2}\right)}{\pi \rho^2} = \frac{P_0}{\pi} \lim_{\rho \to 0} \frac{-(-2)(2\rho)\mathrm{e}^{-2(\rho/w_0)^2}}{w_0^2 (2\rho)} = \frac{2P_0}{\pi w_0^2}, \tag{2.53}$$

Figure 2.3: Three-dimensional illustrations of the non-Gaussian, Lorentzian-Gaussian and Gaussian approximations of the focused beam intensity.

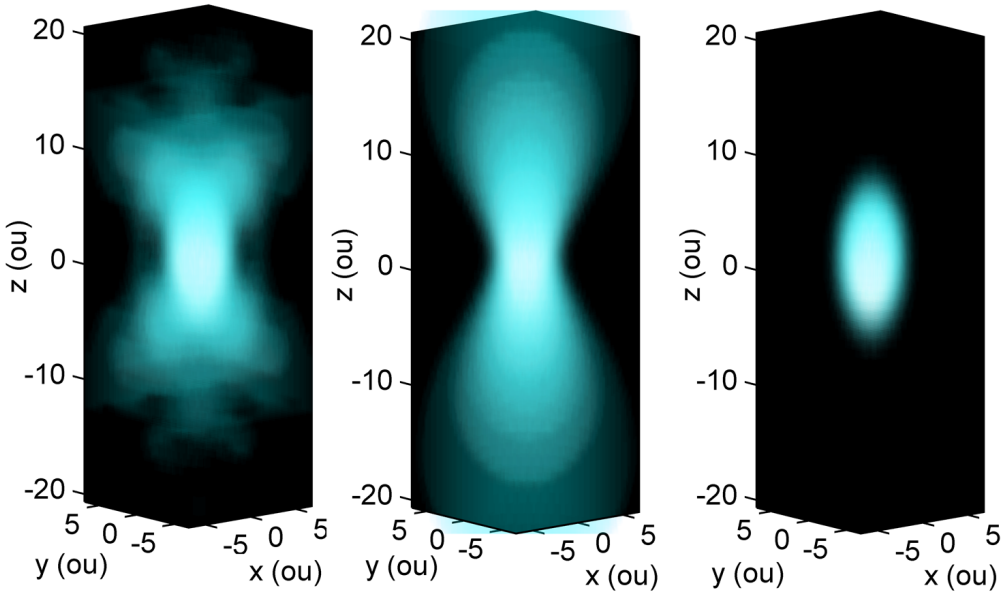

from which the I_0 can be calculated in units of W/m^2 when the laser power P_0 is known. Of course, if the microscope is substantially over-filled, only a certain fraction of laser power is transmitted through the objective aperture. However, this is not a problem in FCS when normalized autocorrelation function is used, and laser intensities are far from the saturation levels of the fluorophore.

Chapter 3

Fluorescence phenomenon

The chapter begins with the overview of how fluorescence originates from the electronic transitions between specific molecular orbitals. The absorption rate of a fluorophore is then formulated under dipole approximation, i.e. in the limit where the excitation electric field is constant over the molecular dimensions [17, p. 306]. Transitions between energy states are explained with Markov chain model for chemical kinetics, leading to equations for time-evolution of fractional occupancies of different molecular states. Finally, the fluorescence emission rate is investigated in the steady state limit.

3.1 Fluorescence

Fluorescence represents one way for light to interact with matter. At its simplest, fluorescence is referred as radiative (photon) decay from the lowest unoccupied molecular orbital (LUMO) to highest occupied molecular orbital (HOMO) of an organic molecule. Jablonski diagram (Fig. 3.1) shows the possible transition paths. The process starts when a photon is absorbed, and an electron is excited from the singlet ground state S_0 to some vibrational state superimposed with singlet excited state S_1 (LUMO state). The efficiency of the absorption process depends on the intensity of the excitation light and current orientation of the absorption dipole moment of the molecule respect to the excitation light polarization (see next section). The electron relaxes to the ground vibrational state of the S_1, where it can decay by either radiatively (photon emission) or non-radiatively via *internal conversion* or vibrational relaxation. Photon yield Q describes the ratio of radiative decay rate (k_r) and total decay rate (k_{10}) from the excited singlet state.

$$Q = \frac{k_r}{k_{10}} = \frac{k_r}{k_r + k_{nr}}, \tag{3.1}$$

where k_{nr} stands for non-radiative decay. Fluorescence lifetime gives the mean duration the fluorophore stays in the excited state, and is measured as

$$\tau_f = \frac{1}{k_{10}} = \frac{1}{k_r + k_{nr}} \tag{3.2}$$

when the effects of collisional and energy transfer quenching are neglected [23]. Since the photon yield and fluorescence lifetime of common fluorophores are usually known

Figure 3.1: Jablonski diagram showing the transitions between the different molecular orbitals.

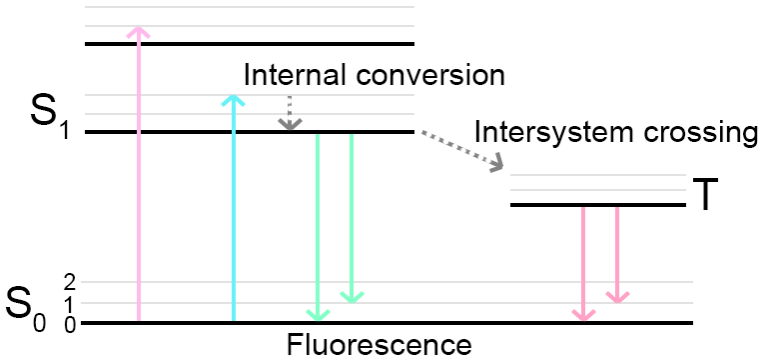

beforehand, it is useful to express the radiative decay rate using these parameters:

$$k_r = k_{10} Q = \frac{Q}{\tau_f}. \tag{3.3}$$

Emission photon will have lower energy than the excitation photon, which is seen as *Stokes shift* between fluorescence absorption and emission spectra. Fluorescence can be *quenched* for example due to the molecular collisions, energy transfer or the presence of molecular oxygen. [17, p. 304-305]

For a certain small probability, the molecule can experience *intersystem crossing*. In this process, the excited state electron has a spin reversal, causing the molecule to change its total electronic spin from 0 to 1. The spin of 1 can have triplet of eigenstates, hence the term *triplet state* (T) transition. After the transition to the triplet state, the electron will eventually go through a spin-forbidden transition back to the singlet ground state with characteristic times ranging from micro- to milliseconds for different fluorophores. These excursions to the triplet state show dark periods in the fluorescence intensity time trace, allowing to study triplet state blinking with FCS. [17, p. 306]

Molecules of interest, such as lipids, do not fluoresce naturally. They have to be labeled with molecules having a favorable molecular structure for LUMO-HOMO transitions. Most fluorophores contain aromatic rings, where the low-energy $\pi \rightarrow \pi^*$ transitions have a very high probability. There are many commercially available fluorophores that can be covalently or non-covalently bonded with a biomolecule, with different excitation and emission properties or applicability to individual experiments such as Förster resonance energy transfer (FRET) studies. Atto-488 (ATTO-TEC), similar to more popular Alexa Fluor dyes, was used for the experiments of this thesis. Atto-488 provides with strong absorption in the range 480 nm to 515 nm with high photostability and displays small Stokes shift, with emission maxima near 520 nm.

3.2 Absorption rate

From now on, the excitation field derived earlier should be distinguished from the emission field with subscript *exc*. The excitation probability of a single fluorophore is proportional to the directional cosine between absorption (transition) dipole moment and excitation field. Rate of energy absorption (power) by a fluorescent molecule with absorption dipole moment $\boldsymbol{\mu}$ is

$$P_{abs} = \frac{\omega}{2}\Im\mathrm{m}\{\boldsymbol{\mu} \cdot \mathbf{E}_{exc}\}, \tag{3.4}$$

while the absorption dipole moment $\boldsymbol{\mu}$ is induced by the same electric excitation field:

$$\boldsymbol{\mu} = \overleftrightarrow{\alpha}\,\mathbf{E}_{exc}, \tag{3.5}$$

where $\overleftrightarrow{\alpha}$ is the tensorial polarizability defined by the molecular framework. Combining these equations gives

$$P_{abs} = \frac{\omega}{2}\Im\mathrm{m}\{\alpha\}|\hat{\boldsymbol{\mu}} \cdot \mathbf{E}_{exc}|^2. \tag{3.6}$$

This equation proves to be useful since it gives the expression for the rate constant of the transition from ground to excited state, k_{01}. In that regime, power has to be divided by the energy of a photon to get the units of 1/s. Unfortunately, the polarizability of a fluorophore is usually not known, and a more feasible parameter is needed. Such a parameter is *absorption cross-section*, defined as

$$\sigma(\omega) = \frac{\langle P_{abs}(\omega)\rangle}{I(\omega)}, \tag{3.7}$$

where the absorbed power is ensemble averaged over all possible dipole orientations and divided by the intensity of excitation field. The absorption cross section is commonly calculated from Beer-Lambert law

$$I(\ell) = I_0\, 10^{\epsilon c \ell} \tag{3.8}$$

where I_0 is the intensity of light arriving in the sample cuvet, c is the molar concentration and ℓ the thickness of the absorbing layer. The parameter ϵ is the *molar extinction coefficient* ($[\epsilon]$ =liter mol^{-1} cm^{-1}), which is related to the absorption cross-section via $\epsilon = \sigma N_A$, where N_A is the Avogadro constant (6.022×10^{23} mol^{-1}). For a fluorophore Atto-488, the extinction coefficient of 80000 M^{-1} cm^{-1} gives a cross-section of 1.33 Å^2 (1 Ångström = 10^{-10} m). [17, p. 315-316]

If the excitation field is approximated as a plane wave, $I \approx \frac{1}{2}n\epsilon_0 c|\mathbf{E}_{exc}|^2$, and then

$$\sigma(\omega) = \frac{\omega}{n\epsilon_0 c}\Im\mathrm{m}\{\alpha\}\langle|\hat{\boldsymbol{\mu}} \cdot \hat{\mathbf{E}}_{exc}|^2\rangle = \frac{\omega}{3n\epsilon_0 c}\Im\mathrm{m}\{\alpha\}|\hat{\boldsymbol{\mu}} \cdot \hat{\mathbf{E}}_{exc}|^2. \tag{3.9}$$

Solving the imaginary part of molecular polarizability and substituting the solution to the equation (3.4) yields the dipole position- and orientation-dependent absorption rate coefficient

$$k_{01}(\mathbf{r}, \hat{\boldsymbol{\mu}}) = \frac{P_{abs}}{\hbar\omega} = \tilde{\sigma} I(\mathbf{r}) \cdot 3|\hat{\boldsymbol{\mu}} \cdot \hat{\mathbf{E}}_{exc}|^2, \tag{3.10}$$

where $\tilde{\sigma} = \sigma/\hbar\omega$ is the absorption cross-section divided by the energy of a photon and $I(\mathbf{r})$ is the intensity distribution. The last term in the equation accounts for the orientational angle between the transition dipole moment and excitation field.

Figure 3.2: Three-level state diagram.

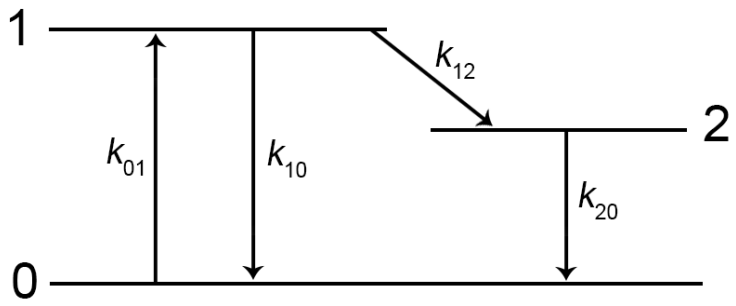

3.3 Rate equations

Figure 3.2 shows a state diagram for general three-level fluorescence process of a single fluorescence emitter. The levels shown in the figure are the singlet ground state ($S_0 = 0$), the first singlet excited state ($S_1 = 1$) and the triplet state ($T = 2$). The occupation of these states in time is described by a continuous-time Markov chain with rate matrix [24]

$$\mathbf{K} = \begin{bmatrix} -k_{01} & k_{10} & k_{20} \\ k_{01} & -(k_{12} + k_{10}) & 0 \\ 0 & k_{12} & -k_{20} \end{bmatrix} \tag{3.11}$$

which is related to the Kolmogorov equation [25, p. 640-642],

$$\frac{\mathrm{d}\mathbf{P}(t)}{\mathrm{d}t} = \mathbf{K}\mathbf{P}(t). \tag{3.12}$$

The elements in transition matrix $\mathbf{P}(t)$ give the conditional probabilities for a fluorophore to occupy state $\Pi = j$ given that it was in state $\Pi = i$ at time zero. Therefore,

$$P_{ij} = \mathrm{P}\{\Pi(t) = j \,|\, \Pi(0) = i\}. \tag{3.13}$$

The solution to Kolmogorov equation is

$$\mathbf{P}(t) = \mathrm{e}^{\mathbf{K}t}, \tag{3.14}$$

which requires calculating matrix exponential for the rate matrix $\mathbf{K}$. The first row of $\mathbf{P}$ corresponds to the probabilities for fluorophore being initially at state S_0, and these have been derived by Widengren *et al* [26]. Solving the matrix exponential in its full analytic form leads to complicated equations that are not practical for the theory of FCS. The equations can be simplified by noting that for a common fluorophore,

$$k_{10} \gg k_{01} > k_{20} > k_{12}. \tag{3.15}$$

Using eigenvalues of the rate matrix,

$$\begin{aligned}\lambda_1 &= 0,\\ \lambda_2 &= -(k_{01}+k_{10}),\\ \lambda_3 &= -\left[k_{20}+\left(\frac{k_{01}}{k_{01}+k_{10}}\right)k_{12}\right],\end{aligned} \tag{3.16}$$

and steady state distributions,

$$\begin{aligned}\overline{S}_0 &= \frac{k_{10}k_{20}}{k_{01}(k_{12}+k_{20})+k_{10}k_{20}},\\ \overline{S}_1 &= \frac{k_{01}k_{20}}{k_{01}(k_{12}+k_{20})+k_{10}k_{20}},\\ \overline{T} &= \frac{k_{01}k_{12}}{k_{01}(k_{12}+k_{20})+k_{10}k_{20}},\end{aligned} \tag{3.17}$$

the elements in the first row of the transition matrix can be written as

$$\begin{aligned}P_{00} = S_0 &= \overline{S}_0 + \frac{\overline{S}_1}{1-\overline{T}}e^{\lambda_2 t} + \frac{\overline{T}}{1-\overline{T}}\overline{S}_0 e^{\lambda_3 t},\\ P_{01} = S_1 &= \overline{S}_1 - \frac{\overline{S}_1}{1-\overline{T}}e^{\lambda_2 t} + \frac{\overline{T}}{1-\overline{T}}\overline{S}_1 e^{\lambda_3 t},\\ P_{02} = T &= \overline{T}\left(1-e^{\lambda_3 t}\right).\end{aligned} \tag{3.18}$$

The second eigenvalue λ_2 characterizes photon *antibunching*, meaning that photons emitted by single fluorophore are separated in time, and there is zero probability to observe a photon instantly from the same molecule. Antibunching can be studied with FCS, but since it has a time-scale in the nanosecond range ($\sim$ fluorescence lifetime), it can be ignored when doing experiments in the slow time-range (µs−ms) [27]. It should also be acknowledged that while the other rate coefficients can be considered as constants, the excitation rate k_{01} has both spatial and angular distribution, which complicates the analysis considerably.

3.4 Steady-state analysis

Photon emission does not happen with a constant rate. Fluorescence emission rate and, therefore, the amount of detected photons will fluctuate in time. Changes between states S_0, S_1 and T occur with characteristic waiting times governed by Poissonian statistics [28]. In steady state, however, the average fluorescence detected from a molecule i is simply proportional to the radiative decay rate times the average probability that a fluorophore is found in its singlet excited state:

$$\overline{F_i} \sim k_r \overline{S}_1 = Q k_{10} \overline{S}_1, \tag{3.19}$$

which is the standard result found in FCS literature. Writing this along with the rate constants yields

$$Qk_{10}\overline{S}_1 = Q\frac{k_{10}k_{01}k_{20}}{k_{01}(k_{12}+k_{20})+k_{10}k_{20}} = Q\frac{k_{01}}{(k_{01}/k_{10})(1+k_{12}/k_{20})+1}. \tag{3.20}$$

Dropping the orientational factor from the excitation rate constant gives $k_{01}(\mathbf{r}) = \tilde{\sigma}I(\mathbf{r})$ where $\tilde{\sigma} = \sigma/\hbar\omega$. Then the steady state photon emission rate reads

$$\overline{F_i}(t) \sim \tilde{\sigma}Q\frac{I(\mathbf{r})}{1+I(\mathbf{r})/I_{sat}}, \tag{3.21}$$

where the factor $I_{sat} = k_{10}/\tilde{\sigma}(1+k_{12}/k_{20})$ is the *saturation intensity* [29]. For high excitation intensities, the fluorescence rate becomes saturated and approaches the value $\tilde{\sigma}QI_{sat}$. Reaching saturation level should be avoided in fluorescence correlation experiment since it can increase photobleaching (chemical inactivation of a fluorophore) and lead to a poor signal-to-noise ratio. Fortunately, the saturation intensities for commonly used fluorophores are rather high. For Atto-488, the natural fluorescence lifetime of 3.2 ns and absorption cross-section of 1.33 Å^2 gives the saturation intensity of 9.57×10^9 W/m^2 at 488 nm wavelength and with negligible intersystem crossing rate. When this is compared to a typical peak excitation intensity of 2.13×10^8 W/m^2 produced by 10 µW laser with Gaussian beam waist diameter of 173 nm ($NA = 1.2$), the fraction I/I_{sat} is only 2.2 %.

Chapter 4

Confocal microscopy

In this chapter, the theoretical foundations of confocal microscopy are outlined. The chapter begins with a brief outlook to the confocal microscope systems used in FCS experiments. Then the characteristics of fluorescent dipolar emission radiation are presented when transferred from object to image space. Finally, the influence of the confocal pinhole on detector point spread (collection efficiency) function is discussed.

4.1 Confocal principle

Confocal optical microscopy is a versatile tool for imaging biological samples, mainly due to its superb contrast and ability to scan thick specimens. In wide-field microscopy (WFM), the entire sample is illuminated by light, and the fluorescence coming from the molecules is collected by a detector or a camera. A confocal microscope, however, uses point illumination by focusing a collimated laser beam with high numerical aperture objective, described in the Chap. 2. This, along with the incorporation of the confocal pinhole allows to obviate the unfocused background light afflicting the traditional wide-field setup. A disadvantage of the confocal principle in imaging purposes is the requirement of observing only one point at a time (linear scanning) or a group of separate points (disc scanning), evidently restricting the temporal resolution of the system.

The pinhole of the confocal microscope provides with three-dimensional discrimination against scattered out-of-focus light, which results in high contrast and resolution. As a downside, smaller pinhole means that less light arrives at the detector, which is why FCS setups commonly use pinholes with radiuses of 2-3 Airy disks. Another reason is that large pinhole has a wide collection efficiency profile (see section 4.3), which makes the detection volume to deviate less from the Gaussian profile commonly assumed in autocorrelation analysis. Thus, the pinhole has a prominent effect on the photon detection probability from a single molecule diffusing in the sample space (section 4.3).

4.2 Dipolar source in image space

The radiation emitted by fluorescent dipole needs to be mapped from object space to image space. *Point spread function* (PSF) tells how the image of a dipolar source molecule

Figure 4.1: Schematic of a confocal epifluorescence microscope with an additional detection path for different polarizations. [30]

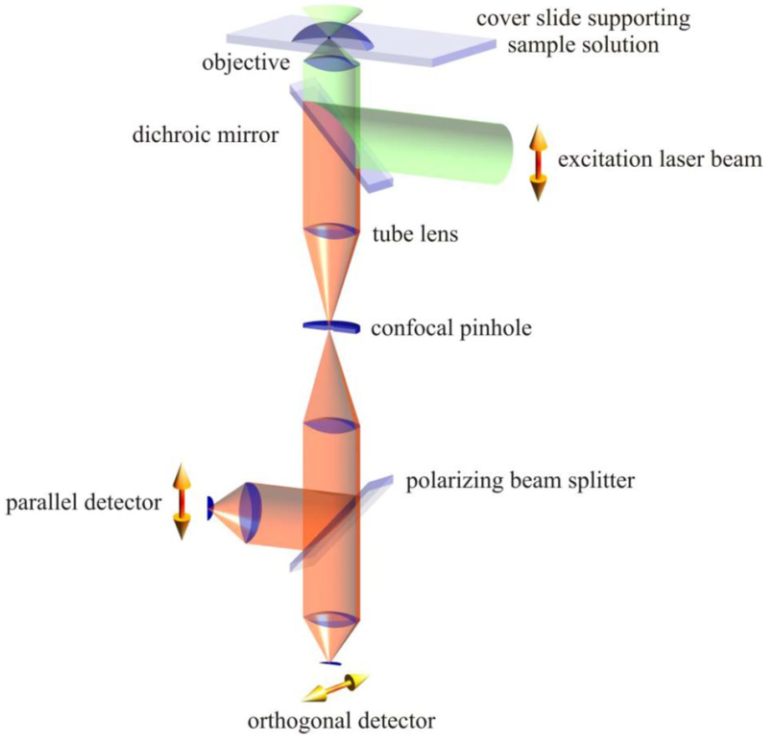

located in point $\mathbf{r}_o$ of object space is spread when arriving to the detector. The electric field radiated by a dipolar particle with dipole moment $\boldsymbol{\mu} = (\mu_x, \mu_y, \mu_z)$ located at the origin of object space is

$$\mathbf{E}_{em}(\mathbf{r}_i, \boldsymbol{\mu}) = \frac{(2\pi)^2}{\epsilon_0 \lambda_{em}^2} \overleftrightarrow{\mathbf{G}}_{PSF}(\mathbf{r}_i) \cdot \boldsymbol{\mu}, \tag{4.1}$$

where $\mathbf{r}_i$ is the field point in image space and $\overleftrightarrow{\mathbf{G}}_{PSF}$ is *Green's dyadic point spread function* [17, p. 90]. Tensor elements of this function involve Bessel integrals similar to those encountered with the focusing of a Gaussian beam (2.41). Since the third row of the Green's dyadic function has only zeros, there is no polarization in the axial direction. Now if the particle is translated from origin to an arbitrary point $\mathbf{r}_o$ in object space, the corresponding image of the dipole will simply translate as

$$\mathbf{E}_{em}(\mathbf{r}_i) \rightarrow \mathbf{E}_{em}(\mathbf{r}_i - \mathbf{M}^T \mathbf{r}_o) \tag{4.2}$$

where the vector

$$\mathbf{M} = \begin{bmatrix} M \\ M \\ M^2 n_i / n_o \end{bmatrix} \tag{4.3}$$

describes the microscope objective magnification on each axis with transverse magnification M. Figure 4.2 demonstrates how the dipole radiation fields in the plane $z = 0$ show

Figure 4.2: Radiation fields of dipolar particles in the focal plane $z = 0$ with $\boldsymbol{\mu} = (\mu_x, 0, 0)$ (left) and $\boldsymbol{\mu} = (0, 0, \mu_z)$ (right).

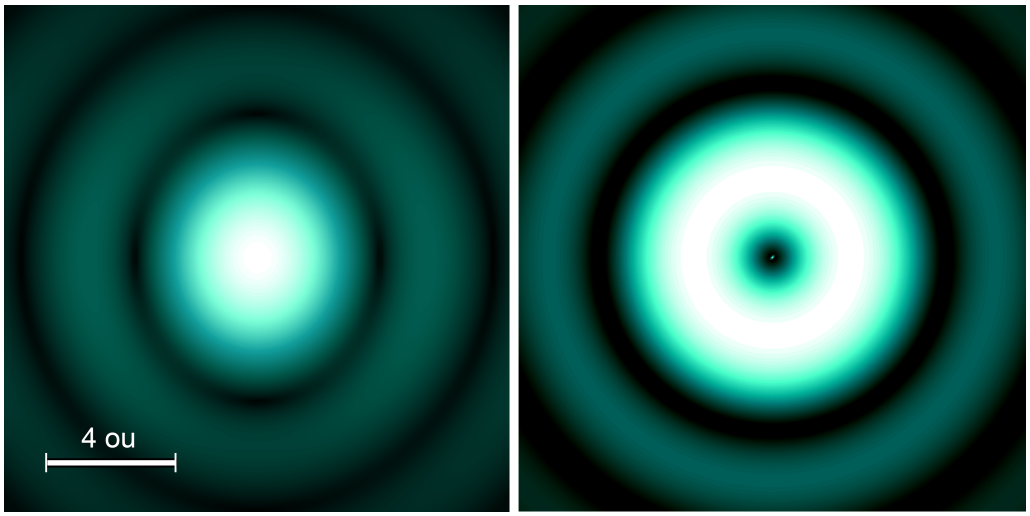

different patterns depending on the dipole moment orientation. While a dipole oriented towards the x-axis has most of its energy surrounding the image space origin, the axially oriented dipole has zero intensity in that point.

Dipolar emission field can also be approximated in terms of Bessel functions in low NA limit. In the focal plane, the magnitude of electric field squared is

$$|\mathbf{E}_{em}(\rho,\, z = 0, \boldsymbol{\mu})|^2 = \frac{\pi^4 NA^4}{\epsilon_0^2 \lambda_{em}^6 M^2 n_o n_i} \left[(\mu_x^2 + \mu_y^2) \left(2\, \frac{J_1(\tilde{v})}{\tilde{v}} \right)^2 + 2\mu_z^2 \left(\frac{NA}{n_o} \right)^2 \left(2\, \frac{J_2(\tilde{v})}{\tilde{v}} \right)^2 \right], \quad (4.4)$$

where $\tilde{v} = k\rho \sin\theta_{max}/M$. In axial direction,

$$|\mathbf{E}_{em}(\rho = 0, z, \boldsymbol{\mu})|^2 = \frac{\pi^4 NA^4}{\epsilon_0^2 \lambda_{em}^6 M^2 n_o n_i} (\mu_x^2 + \mu_y^2) \left(\frac{\sin(\tilde{u}/4)}{\tilde{u}/4} \right)^2, \quad (4.5)$$

where $\tilde{u} = (n_o/n_i\, M^2) kz \sin^2\theta_{max}$. It turns out, however, that Bessel function approximations are much more accurate in high NA limit than its analogous equations for the focused Gaussian laser beam. In order to calculate directional energy flux density at the detector, it is sufficient to exclude the magnetic field and calculate the magnitude of the time-averaged Poynting vector using only the electric field:

$$S_{em} = \frac{1}{2} \epsilon_0 n_i c |\mathbf{E}_{em}|^2, \quad (4.6)$$

which is the *dipole point spread function* (dipole PSF), describing the spreading of a dipolar point source in image space.

Figure 4.3: The calculated point spread functions for a confocal system with pinhole sizes 30 µm, 15 µm and 5 µm (from left to right).

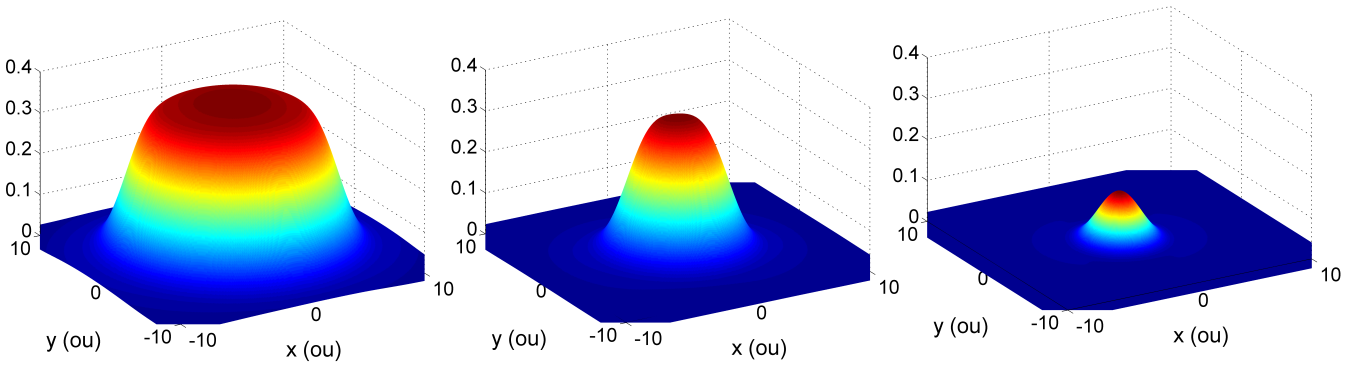

4.3 Point spread function

Detector point spread function (or collection efficiency function, CEF) $\Omega(\mathbf{r}_o)$ is calculated by convolving the dipole emitter PSF with the circular pinhole of the confocal system. The procedure is equal to integrating time-averaged Poynting vector of the dipole radiation over the pinhole area. The detector PSF should represent the probability of one photon passing the confocal aperture, for every dipole emitter position $\mathbf{r}_o = (x_o, y_o, z_o)$ in object space. The normalization should be done by using the total power radiated by the dipole,

$$\langle P_{em} \rangle = \frac{4\pi^3 \mu^2 c}{3\epsilon_0 \lambda_{em}^4}. \tag{4.7}$$

Detector PSF then becomes

$$\Omega(\mathbf{r}_o, \boldsymbol{\mu}) = \frac{1}{\langle P_{em} \rangle} \iint_{det} S_{em}(\mathbf{r}_i - \mathbf{M}^T \mathbf{r}_o, \boldsymbol{\mu})\, \mathrm{d}x_i\, \mathrm{d}y_i, \tag{4.8}$$

where the pinhole is located in the plane $\mathbf{r}_i = (x_i, y_i, 0)$. Figure 4.3 shows the detector PSF for pinhole sizes of 30 µm, 15 µm and 5 µm (2, 1 and 0.33 Airy disks, respectively), with dipole moment vector averaged over all possible orientations. When pinhole size increases, the detector PSF becomes a smeared image of the pinhole.

If there is no correlation between the transition dipole moment between absorption and emission of a photon, i.e. with the infinitely fast rotational diffusion, the total point spread function of the confocal system is the product of the excitation field and detector PSF:

$$TOTAL\ PSF = I(\mathbf{r}_o) \times \Omega(\mathbf{r}_o) = \Theta(\mathbf{r}_o), \tag{4.9}$$

which is sometimes referred as *molecule detection function* (MDF). One should emphasize that the simple product of excitation and detector point spread functions is not possible in rotationally anisotropic samples, which is due to the correlation between absorption and emission dipoles coupled by rotational diffusion. The terms can be separated only in

the limit of infinitely fast rotational diffusion. In highly compressed lipid monolayers, rotational mobility should become rather restricted but still the time-scales of rotational motions are much shorter than the translational diffusion of triplet kinetics (see section 5.3).

Chapter 5

Fluorescence Correlation Spectroscopy

This chapter focuses on the autocorrelation analysis, which is the essence of FCS. The approach represented here differs from the usual deterministic treatment, which relates the concentration fluctuations in sample volume to the diffusion equation. Here, the stochastic nature of the measured fluorescence is taken into account by incorporating probabilities for individual molecules to translate, rotate and chemically react. In the limit of large sample dimensions in comparison with the detection volume, and with considerable amount of fluorophores, these stochastic equations yield the same results as the fluctuation analysis commonly found in FCS literature [31, 32]. Technical aspects of FCS, such as computational performance or signal-to-noise characteristics, are not discussed.

5.1 Derivation of the autocorrelation function

Measured fluorescence intensity is a random stochastic signal that fluctuates in time owing to changes in myriad of different variables such as particle position, dipole moment orientation, population of the triplet state, background radiation and properties of the experimental setup. The only approach to treat such a complex signal is via the tools of statistical analysis. The way to characterize any statistical signal is to use probability theory. Fluorescence correlation analysis relies on the fact that measured signal is *stationary* at least in *wide sense*, meaning that its 1- and 2-fold probability densities do not change in time, and its statistical properties can be deduced from one single (sufficiently long) realization of the process. Assumption of stationarity is not strictly true if the properties of the fluorophores change in time due to the statistical aging effect, for example [33].

Let's suppose there is a sample of N molecules which can fluctuate between M different states via chemical reaction or photophysical conversions. Total fluorescence signal from all molecules in the sample is the sum of individual intensities:

$$F(t) = \sum_{\gamma=1}^{M} \sum_{i=1}^{N_\alpha} F_{\gamma,i}(t) \tag{5.1}$$

for a negligible background intensity. Variance of the signal is

$$\langle [\delta F(t)]^2 \rangle_t = \langle [F(t) - \langle F(t) \rangle_t]^2 \rangle_t = \langle F(t)^2 \rangle_t - \langle F(t) \rangle_t^2, \tag{5.2}$$

where brackets denote the *temporal average* of the signal over t,

$$\langle F(t)\rangle_t = \lim_{T\to\infty} \frac{1}{T}\int_0^T F(t)\,\mathrm{d}t. \tag{5.3}$$

Normalized *fluorescence autocorrelation function* of the signal is defined as

$$G(\tau) = \frac{\langle F(t)F(t+\tau)\rangle_t}{\langle F(t)\rangle_t^2} = \frac{\sum_{\alpha,\beta}\langle F_\alpha(t)F_\beta(t+\tau)\rangle_t}{\langle\sum_\gamma F_\gamma(t)\rangle_t^2}, \tag{5.4}$$

which describes the self-similarity of the signal after lag-time τ and is the sum of intermediate auto- and cross-correlations of all different states. The unnormalized autocorrelation functions $G'_{\alpha\beta}(\tau)$ consist of the terms in the numerator. Another form of the autocorrelation function is *fluorescence fluctuation autocorrelation function*, given by [10, p. 363]

$$g(\tau) = \frac{\langle \delta F(t)\delta F(t+\tau)\rangle_t}{\langle F(t)\rangle_t^2} = G(\tau) - 1. \tag{5.5}$$

This relationship follows from the fact that the standard deviation of the signal, $\langle \delta F(t)\rangle_t$, is zero. $G(\tau)$ and $g(\tau)$ are often used simultaneously in literature since they only differ by an addition of a constant.

Assumption of an ideal chemical solution yields that fluorescence signals detected from different molecules are uncorrelated and contribute to the autocorrelation only by some constant. Then

$$\begin{aligned} G'_{\alpha\beta}(\tau) = \langle F_\alpha(t)F_\beta(t+\tau)\rangle_t &= \langle \sum_{j,k} F_{\alpha,j}(t)F_{\beta,k}(t+\tau)\rangle_t \\ &= \langle N_\alpha F_{\alpha,i}(t)F_{\beta,i}(t+\tau)\rangle_t + \langle N_\alpha(N_\beta - 1)F_{\alpha,i}(t)F_{\beta,i}(t)\rangle_t \\ &= \langle N_\alpha\rangle\langle F_{\alpha,i}(t)F_{\beta,i}(t+\tau)\rangle_t + \langle N_\alpha\rangle(\langle N_\beta\rangle - 1)\langle F_{\alpha,i}(t)\rangle_t\langle F_{\beta,i}(t)\rangle_t, \end{aligned} \tag{5.6}$$

where $F_{\alpha,i}$ and $F_{\beta,i}$ are considered as signals from any of the molecules being in state α or β. There can be ideally a pair of correlated fluorescence detection events from N_α molecules and from $N_\alpha(N_\beta - 1)$ different molecules [4]. When the limiting case of only one molecular state is considered, the normalized autocorrelation function reduces to

$$G(\tau) = \frac{\langle F_i(0)F_i(\tau)\rangle}{N\langle F_i\rangle^2} + 1 - \frac{1}{N}. \tag{5.7}$$

The term $1/N$ may seem peculiar but can be explained with photon antibunching. As discussed, the probability to detect a second photon immediately (zero lag) after detecting a photon from a same molecule is zero since fluorophore needs to be excited to its first singlet state. However, it is possible to detect a photon immediately from another molecule. Therefore, if one has only one molecule in the system, $1 - \frac{1}{1} = 0$ and zero probability is observed at $\tau = 0$. On the other hand, if the number of molecules is substantial, $1/N \to 0$. This is indeed the situation in most experimental configurations and will be assumed from now on.

Now the stationarity of the fluorescence signal is invoked, and the origin of time is choosed to be at zero ($t = 0$). Also, it is assumed that the signal is *ergodic*, meaning that the temporal averages can be substituted with ensemble averages. For convenience, let's focus on unnormalized autocorrelation function for a single fluorophore. Ensemble-averaging leads to a quite complicated correlation function

$$\langle F_{\alpha,i}(0)F_{\beta,i}(\tau)\rangle = \int k_{r,\alpha}k_{r,\beta}\Omega(\mathbf{r}', \hat{\boldsymbol{\mu}}', 0)\Omega(\mathbf{r}, \hat{\boldsymbol{\mu}}, \tau)\cdot$$

$$p_\alpha(\mathbf{r}', \hat{\boldsymbol{\mu}}', 0) \cdot p_{\alpha\beta}(\mathbf{r}, \hat{\boldsymbol{\mu}}, \tau \,|\, \mathbf{r}', \hat{\boldsymbol{\mu}}', 0)\, \mathrm{d}\hat{\boldsymbol{\mu}}\, \mathrm{d}\hat{\boldsymbol{\mu}}'\, \mathrm{d}\mathbf{r}\, \mathrm{d}\mathbf{r}', \quad (5.8)$$

which is the product of radiative decay rates of the different states, detection efficiencies and probability density functions integrated over all possible initial and final fluorophore positions and transition dipole moments. The problem of interest now is to find the conditional probability distribution $p_{\alpha\beta}(\mathbf{r}, \hat{\boldsymbol{\mu}}, \tau \,|\, \mathbf{r}', \hat{\boldsymbol{\mu}}', 0)$ that a photon is detected at time τ from state β with location $\mathbf{r}$ and transition dipole moment orientation $\hat{\boldsymbol{\mu}}$, given that there was a photon detected at time zero from state α with the corresponding parameters $\mathbf{r}'$ and $\hat{\boldsymbol{\mu}}'$.

5.2 Diffusion equation

It follows from the theory of partial differential equations that the conditional probability distribution looked for in the previous section is given as a solution to the *diffusion equation* coupled with chemical kinetics. When the diffusional properties of the molecule are independent of the molecular state, the diffusion equation reads

$$\frac{\partial p_{\alpha\beta}}{\partial t} = D_T \nabla^2 \, p_{\alpha\beta} + D_R L^2 \, p_{\alpha\beta} + \sum_{\gamma=1}^{M} K_{\alpha\gamma} p_{\gamma\beta}, \quad (5.9)$$

where D_T and D_R are the translational and rotational diffusion coefficients, respectively, ∇ is the gradient operator of the space and L is the angular momentum operator. The equation is to be solved with the boundary conditions $p(\mathbf{r}, 0) = \delta(\mathbf{r} - \mathbf{r}')$ and $p(\hat{\boldsymbol{\mu}}, 0) = \delta(\hat{\boldsymbol{\mu}} - \hat{\boldsymbol{\mu}}')$, molecule initially being at state α. A clear simplification can be made when it is accepted that the orientation of the transition dipole moment is independent of the location, which is true if the sample is homogeneous. The joint probability is then just a multiplication of independent probabilities, given as

$$p_{\alpha\beta}(\mathbf{r}, \hat{\boldsymbol{\mu}}, t \,|\, \mathbf{r}', \hat{\boldsymbol{\mu}}', 0) = p(\mathbf{r}, t \,|\, \mathbf{r}', 0) \cdot p(\hat{\boldsymbol{\mu}}, t \,|\, \hat{\boldsymbol{\mu}}', 0) \cdot P_{\alpha\beta}(t), \quad (5.10)$$

where $P_{\alpha\beta}(t)$ is the transition probability from state α to β. In the following sections translational and rotational contributions are treated separately, and then the chemical kinetics are applied to the triplet state blinking.

5.3 Rotational diffusion

It was discussed that when the excitation light is polarized parallel to the absorption dipole moment of the fluorophore, the absorption becomes most probable. This relationship was

incorporated to the absorption rate constant k_{01}. However, in most cases this probability is only introduced as a multiplicative term in Eq. 5.8. Indeed, for moderate laser intensities, [34]

$$k_{10}\overline{S}_1(\mathbf{r}, \hat{\boldsymbol{\mu}}) \approx 3|\hat{\boldsymbol{\mu}} \cdot \hat{\mathbf{E}}_{exc}|^2 \frac{\tilde{\sigma} I(\mathbf{r})}{1 + I(\mathbf{r})/I_{sat}}. \tag{5.11}$$

If $p(\hat{\boldsymbol{\mu}}, t)$ is the probability density of having a molecule with orientation $\hat{\boldsymbol{\mu}}$ at time t, then $p(\hat{\boldsymbol{\mu}}, t)\mathrm{d}\hat{\boldsymbol{\mu}} = p(\hat{\boldsymbol{\mu}}, t) \sin\theta \, \mathrm{d}\theta\mathrm{d}\phi$ is the probability of having an orientation inside a solid angle. For excitation polarization chosen to be along x-axis, the directional absorption probability using spherical coordinates is

$$3|\hat{\boldsymbol{\mu}} \cdot \hat{\mathbf{E}}_{exc}|^2 = 3 \sin^2\theta \cos^2\phi. \tag{5.12}$$

It is assumed that transition dipole moment is fixed in the molecular framework and does not re-orientate between absorption and emission. Then the rotations of the dipole moment are only due to the rotations of the molecule. When the molecule is only able to rotate around a unit sphere, angular momentum operator simplifies to the one corresponding to the rotational diffusion operator in the unit sphere, yielding solutions as a sum of spherical harmonics. More complicated geometries require rotational diffusion tensor describing the rotation around each molecular axis.

Little evidence of rotational diffusion of single lipids in model membranes exists due to the experimental difficulties. Honigmann et al. measured rotational diffusion coefficients in pure liquid-disordered (L_d) lipid bilayer as $2.9 - 1.4 \times 10^7 \mathrm{s}^{-1}$ depending on the solvent used for membrane preparation [35]. For very high lateral pressures in a Langmuir monolayer, rotational diffusion could in principle approach these values. For example, the introduction of proteins into the hydrophobic core of a bilayer restricts the rotational diffusion, increasing the measured anisotropy.

Traditionally, rotational diffusion is studied with fluorescence depolarization experiments, where it is required that rotational diffusion has the same time scale as fluorescence decay [36, 37]. In FCS experiments, fast reorientation of the transition dipole moment between absorption and emission can be taken into account by incorporating fourth-order correlation function or by ensemble averaging with fluorescence decay curve as a weight function [3, 34, 38]. From now on, it is assumed that the system exhibits zero anisotropy, molecules rotate very rapidly and the position of transition dipole moment vector is weakly correlated with the positions in earlier time. Thus, the only task involving transition dipole moment is to average detection efficiency function Ω over all possible dipole orientations using Eq. 5.12. By also noting that $p(\hat{\boldsymbol{\mu}}, t = 0) = 1/4\pi$ finally yields

$$\Omega(\mathbf{r}) = \frac{3}{4\pi} \int_0^{2\pi} \int_0^{\pi} \Omega(\mathbf{r}, \hat{\boldsymbol{\mu}}) \sin^3\theta \cos^2\phi \, \mathrm{d}\theta\mathrm{d}\phi. \tag{5.13}$$

5.4 Translational diffusion

For two-dimensional diffusion, $\mathbf{r} = (x, y)$, and the solution for the translational diffusion equation is

$$p(\mathbf{r} - \mathbf{r}', t) = \frac{1}{4\pi D_T t} \mathrm{e}^{\frac{-|\mathbf{r}-\mathbf{r}'|^2}{4D_T t}}. \tag{5.14}$$

In addition, $p(\mathbf{r}, 0)\mathrm{d}\mathbf{r} = \mathrm{d}\mathbf{r}/A$ gives the probability for a molecule to be inside an infinitesimal area element $\mathrm{d}\mathbf{r} = \mathrm{d}x\mathrm{d}y$ of a sample with total area A. The solution to the translational diffusion equation signifies the fact that the molecule is located exactly at $\mathbf{r} = \mathbf{r}'$ at time zero, and at the later times the location becomes more uncertain as the function spreads. Functional form the solution is Gaussian, and thus the variance is

$$\sigma^2(t) = \left[\mathbf{r}(t) - \mathbf{r}'\right]^2 = 4D_T t \tag{5.15}$$

when the diffusional motion is not hindered. It follows that the translational diffusion constant can be written as [39]

$$D_T = \frac{w(z)^2}{4\tau_D}, \tag{5.16}$$

where w is the effective beam radius and τ_D is the *diffusion time*, which quantifies the average time a fluorophore spends in the detection volume. Diffusion times can be measured from FCS experiment even when w is unknown. However, to calculate diffusion constant from diffusion time, the beam waist radius $w(0) = w_0$ has to be experimentally measured. This can be achieved by calibrating the system using a fluorophore with known diffusion coefficient.

5.5 Triplet kinetics

For triplet kinetics, the fast cycling between the ground and excited singlet states (antibunching) can be neglected. Then the transition to the dark state can be described with simple first-order kinetics,

$$S_0 + S_1 = S \rightarrow T, \tag{5.17}$$

where singlet state S is the state 1 and T is state 2. The rate matrix of the system is

$$\mathbf{K} = \begin{bmatrix} -\eta k_{12} & k_{20} \\ \eta k_{12} & -k_{20} \end{bmatrix}, \tag{5.18}$$

where $\eta = k_{01}/(k_{01} + k_{10})$ signifies the fact that the transition to the triplet state can occur only from the state S_1. In other words, the probability of transition to the triplet state increases with increasing absorption rate coefficient. With the same argument, the radiative decay of the combined singlet state is $k_{r,1} = \eta Q_1 k_{10}$. In the limit where translational diffusion is independent of the triplet state blinking, the analysis becomes equivalent to the one already done in Section 3.3 for three-state system. In the case of individual diffusion coefficients for different states, the probability distribution should be solved in Fourier space. [40, 41]

The photon yield Q_2 and thus the radiative decay rate of the triplet state is zero, which allows to drop all correlation terms in 5.6 except G'_{11}. Then the only relevant transition probability is [10, p. 284]

$$P_{11}(\mathbf{r}, t) = \overline{S}(\mathbf{r})\left(1 + \frac{\overline{T}(\mathbf{r})}{1 - \overline{T}(\mathbf{r})}\mathrm{e}^{-t/\tau_T(\mathbf{r})}\right), \tag{5.19}$$

where

$$\overline{S}(\mathbf{r}) = \frac{k_{01}(\mathbf{r}) + k_{10}}{k_{01}(\mathbf{r})(k_{20} + k_{12}) + k_{10}k_{20}},$$
$$\overline{T}(\mathbf{r}) = \frac{k_{01}(\mathbf{r})k_{12}}{k_{01}(\mathbf{r})(k_{20} + k_{12}) + k_{10}k_{20}}, \tag{5.20}$$
$$\tau_T(\mathbf{r}) = (k_{20} + \eta k_{12})^{-1} = \left(k_{20} + \frac{k_{01}(\mathbf{r})}{k_{01}(\mathbf{r}) + k_{10}}k_{12}\right)^{-1}$$

are the singlet and triplet state steady state populations and triplet state lifetime, respectively. All parameters are dependent on the position in the sample space through $k_{01}(\mathbf{r})$. Using $p_1(\mathbf{r}', 0) = \overline{P}_{11}(\mathbf{r}')/A$ allows to write

$$\langle N_1\rangle\langle F_{1,i}(0)F_{1,i}(\tau)\rangle = \frac{\langle N_1\rangle}{A}\int k_{r,1}(\mathbf{r}')k_{r,1}(\mathbf{r})\,\Omega(\mathbf{r}')\Omega(\mathbf{r})\,\overline{P}_{11}(\mathbf{r}')P_{11}(\mathbf{r},\tau)p(\mathbf{r}-\mathbf{r}',\tau)\mathrm{d}\mathbf{r}\,\mathrm{d}\mathbf{r}'$$
$$= \langle c\rangle\int k_{10}^2Q^2\eta(\mathbf{r}')\eta(\mathbf{r})\Omega(\mathbf{r}')\Omega(\mathbf{r})\,\overline{S}(\mathbf{r}')\overline{S}(\mathbf{r})\left(1 + \frac{\overline{T}(\mathbf{r})}{1-\overline{T}(\mathbf{r})}\mathrm{e}^{-\tau/\tau_T(\mathbf{r})}\right)p(\mathbf{r}-\mathbf{r}',\tau)\mathrm{d}\mathbf{r}\,\mathrm{d}\mathbf{r}'$$
$$= \frac{(\tilde{\sigma}\,Q)^2\langle c\rangle}{4\pi D_T\tau}\int\Theta(\mathbf{r}')\Theta(\mathbf{r})\left(1 + \frac{\overline{T}(\mathbf{r})}{1-\overline{T}(\mathbf{r})}\mathrm{e}^{-\tau/\tau_T(\mathbf{r})}\right)\mathrm{e}^{\frac{-|\mathbf{r}-\mathbf{r}'|^2}{4D_T\tau}}\mathrm{d}\mathbf{r}\,\mathrm{d}\mathbf{r}', \tag{5.21}$$

where

$$\Theta(\mathbf{r}) = k_{10}\eta(\mathbf{r})\Omega(\mathbf{r})\overline{S}(\mathbf{r}) = \frac{I(\mathbf{r})\Omega(\mathbf{r})}{1 + I(\mathbf{r})/I_{sat}}. \tag{5.22}$$

With low laser intensities, the optical saturation is negligible, and MDF reduces to the total point spread function of the confocal system. It was also assumed that $\langle N_1\rangle/A = \langle c\rangle$ represents the overall sample concentration, which is justified by the fact that triplet transition is possible only when a fluorophore is passing through the confocal volume ($N \approx \langle N_1\rangle \gg \langle N_2\rangle$). Again, since the photon yield Q_2 of the triplet state is zero, the square of the average fluorescence intensity required for normalization is

$$\langle F(t)\rangle^2 = \langle N_1F_{1,i}(t)\rangle^2$$
$$= \frac{\langle N_1\rangle^2}{A^2}\left(\int k_{10}Q\eta(\mathbf{r})\Omega(\mathbf{r})\overline{S}(\mathbf{r})\mathrm{d}\mathbf{r}\right)^2 = (\tilde{\sigma}\,Q\,\overline{c})^2\left(\int\Theta(\mathbf{r})\mathrm{d}\mathbf{r}\right)^2. \tag{5.23}$$

Finally, the normalized autocorrelation can be calculated from

$$G(\tau) = 1 + \frac{1}{\langle c\rangle\,(4\pi D_T\tau)}\frac{\displaystyle\int\Theta(\mathbf{r}')\Theta(\mathbf{r})\left(1 + \frac{\overline{T}(\mathbf{r})}{1-\overline{T}(\mathbf{r})}\mathrm{e}^{-\tau/\tau_T(\mathbf{r})}\right)\mathrm{e}^{\frac{-|\mathbf{r}-\mathbf{r}'|^2}{4D_T\tau}}\mathrm{d}\mathbf{r}\,\mathrm{d}\mathbf{r}'}{\displaystyle\left(\int\Theta(\mathbf{r})\mathrm{d}\mathbf{r}\right)^2}. \tag{5.24}$$

5.6 Analytic form of the autocorrelation function

Now it is investigated if the equation 5.24 can in any way be solved analytically. Widengren et al. showed that replacing the exact position-dependent forms of the triplet state lifetime and steady state populations with spatial averages do not lead into considerable error as long as the detection point spread function is narrow, i.e. when the pinhole size remains small enough [26]. At that limit, the term accounting for the triplet state blinking can be pulled out of the integral, and

$$G(\tau) = 1 + \frac{1 - \overline{T} + \overline{T}\mathrm{e}^{-\tau/\tau_T}}{\langle c \rangle (1 - \overline{T})(4\pi D_T \tau)} \frac{\int \Theta(\mathbf{r}')\Theta(\mathbf{r})\mathrm{e}^{\frac{-|\mathbf{r}-\mathbf{r}'|^2}{4D_T\tau}} \mathrm{d}\mathbf{r}\,\mathrm{d}\mathbf{r}'}{\left(\int \Theta(\mathbf{r})\mathrm{d}\mathbf{r}\right)^2}. \tag{5.25}$$

The experiments of the thesis were performed using *z-scan FCS*, meaning that the planar monolayer sample was scanned in multiple steps in the axial direction. Z-scan allows to find the minimal diffusion time achieved in the beam waist of the laser focus. The functional form of the autocorrelation function used to fit the experimental data exploits the Lorentzian-Gaussian approximation derived in section 2.6 [42]. For sufficiently large pinhole sizes (several wavelengths) and low laser intensities (no saturation), molecule detection function can be approximated as

$$\Theta(x, y, z) = I_0 \frac{w_0^2}{w(z)^2} \mathrm{e}^{-2\frac{x^2+y^2}{w(z)^2}}, \tag{5.26}$$

where $w(z)$ gives the effective beam radius at any focal depth z. For a planar system, $\mathrm{d}\mathbf{r} = \mathrm{d}x\mathrm{d}y$, and in the limit $\tau \to 0$, the fraction of integrals

$$\frac{\left(\int \Theta(x, y, z)\,\mathrm{d}x\mathrm{d}y\right)^2}{\int \Theta(x, y, z)^2\,\mathrm{d}x\mathrm{d}y} = \frac{\left(\int \mathrm{e}^{-2\frac{x^2+y^2}{w(z)^2}}\,\mathrm{d}x\mathrm{d}y\right)^2}{\int \mathrm{e}^{-4\frac{x^2+y^2}{w(z)^2}}\,\mathrm{d}x\mathrm{d}y} = \pi w(z)^2 = A_{eff}(z) \tag{5.27}$$

quantifies the *effective focal area* [43]. Now the equation 5.25 can be solved analytically as

$$\begin{aligned} G(\tau, z) &= 1 + \frac{1 - \overline{T} + \overline{T}\mathrm{e}^{-\tau/\tau_T}}{\langle c \rangle (1 - \overline{T})(4\pi D_T \tau)} \cdot \frac{4D_T\tau}{w(z)^2 + 4D_T\tau} \\ &= 1 + \left(1 - \overline{T} + \overline{T}\mathrm{e}^{-\tau/\tau_T}\right) \frac{1}{\langle c \rangle \pi w(z)^2 (1 - \overline{T})} \frac{1}{1 + 4D_T\tau/w(z)^2} \\ &= 1 + \left(1 - \overline{T} + \overline{T}\mathrm{e}^{-\tau/\tau_T}\right) \frac{1}{N_{eff}(z)(1 - \overline{T})} \frac{1}{1 + \tau/\tau_D(z)}, \end{aligned} \tag{5.28}$$

where the relevant parameters to obtain from a FCS experiment are [42]

$$N_{eff}(z) = \langle c \rangle A_{eff}(z) = \pi w_0^2 \left(1 + \frac{z^2}{z_0^2}\right) = N_0 \left(1 + \frac{\lambda_{exc}^2 z^2}{\pi^2 w_0^4}\right),$$
$$\tau_D(z) = \frac{w_0^2}{4D_T} \left(1 + \frac{\lambda_{exc}^2 z^2}{\pi^2 w_0^4}\right) = \tau_{min} \left(1 + \frac{\lambda_{exc}^2 z^2}{\pi^2 w_0^4}\right). \tag{5.29}$$

The minimums of diffusion time $\tau_D(0) = \tau_{min}$ and average number of particles in the focus $N_{eff}(0) = N_0$ are found in the beam waist. The equation (5.28) and the definitions in Eq. (5.29) form the basis of the autocorrelation curve fitting procedure in the experimental part. If the triplet blinking term is disregarded ($G = G_D$), the remaining part approaches $G_D(0) = 1 + 1/N_{eff}(z)$ when $\tau \to 0$. On the other hand, the whole autocorrelation function approaches $G(0) = 1 + 1/N_{eff}(z)(1 - \overline{T})$, where the denominator corresponds to the average number of molecules in the beam focus times the steady state population fraction of the singlet states, $\overline{S} = 1 - \overline{T}$. One finds that $\frac{G_D(\tau_D)-1}{G_D(0)-1} = 1/2$.

For the case of two fluorescent species a and b laterally diffusing through the detection volume, Eq. (5.28) can be expanded as

$$G(\tau, z) = 1 + \left(1 - \overline{T} + \overline{T} \mathrm{e}^{-\tau/\tau_T}\right) \frac{1}{N_{eff}(z)(1 - \overline{T})} \left(\frac{1}{1 + \tau/\tau_{Da}(z)} + \frac{1}{1 + \tau/\tau_{Db}(z)}\right), \tag{5.30}$$

where τ_{Da} and τ_{Db} correspond to the diffusion times of two fluorescent species with different diffusing properties, and Amp is the amplitude of autocorrelation corresponding to faster diffusing species τ_{Da}. This form of the autocorrelation function was incorporated in order to account for the domain migration in Langmuir monolayer experiments.

5.7 Numerical calculations

Autocorrelation functions were modeled using MATLAB by first calculating the non-Gaussian intensity profile ($NA = 1.2$, $n = 1.333$) and detector PSF ($M = 60$, pinhole radius of 30 µm) in a 200×200 grid with dimensions of 750×750 nm (x, y) in object space units and 13 axial steps with step-size of 200 µm in image space units (≈ 74 nm in object space). The product between the convolution $\Theta(\mathbf{r}) \otimes p(\mathbf{r}, \tau)$ and the remaining MDF and triplet terms gives a function that can be finally integrated in the sample space. Atto-488 fluorophore was modeled with wavelengths of 488 nm for excitation and 515 nm for emission, and triplet parameters $k_{20}^{-1} = 10$ µs, $k_{12}^{-1} = 50$ µs. Other parameters for Atto-488 that were kept fixed during the analysis are found in section 3.4. Diffusion coefficient was set as 7.2×10^{-12} m^2/s, which results in diffusion time of ~ 1 ms in the beam waist. The concentration of the fluorophores was 5×10^{12} molecules/m^2.

Various model parameters were obtained by fitting the analytic function 5.28 to the calculated autocorrelation curves. Table 5.1 summarizes these fittings when studying optical saturation (A) and triplet state blinking (B) separately. With increasing laser power,

Figure 5.1: Calculated autocorrelation functions. Red curves denote the functions free of triplet state blinking and optical saturation. (A) Effect of optical saturation (no triplet blinking) and (B) triplet state blinking with varying laser power. (B) Effect of with varying (C) Autocorrelation functions for various axial positions. The negative z-values are omitted since the profile is symmetric. (D) Diffusion time τ_D and effective number of molecules N_{eff} as a function of axial position ($P_0 = 10\,\mu W$).

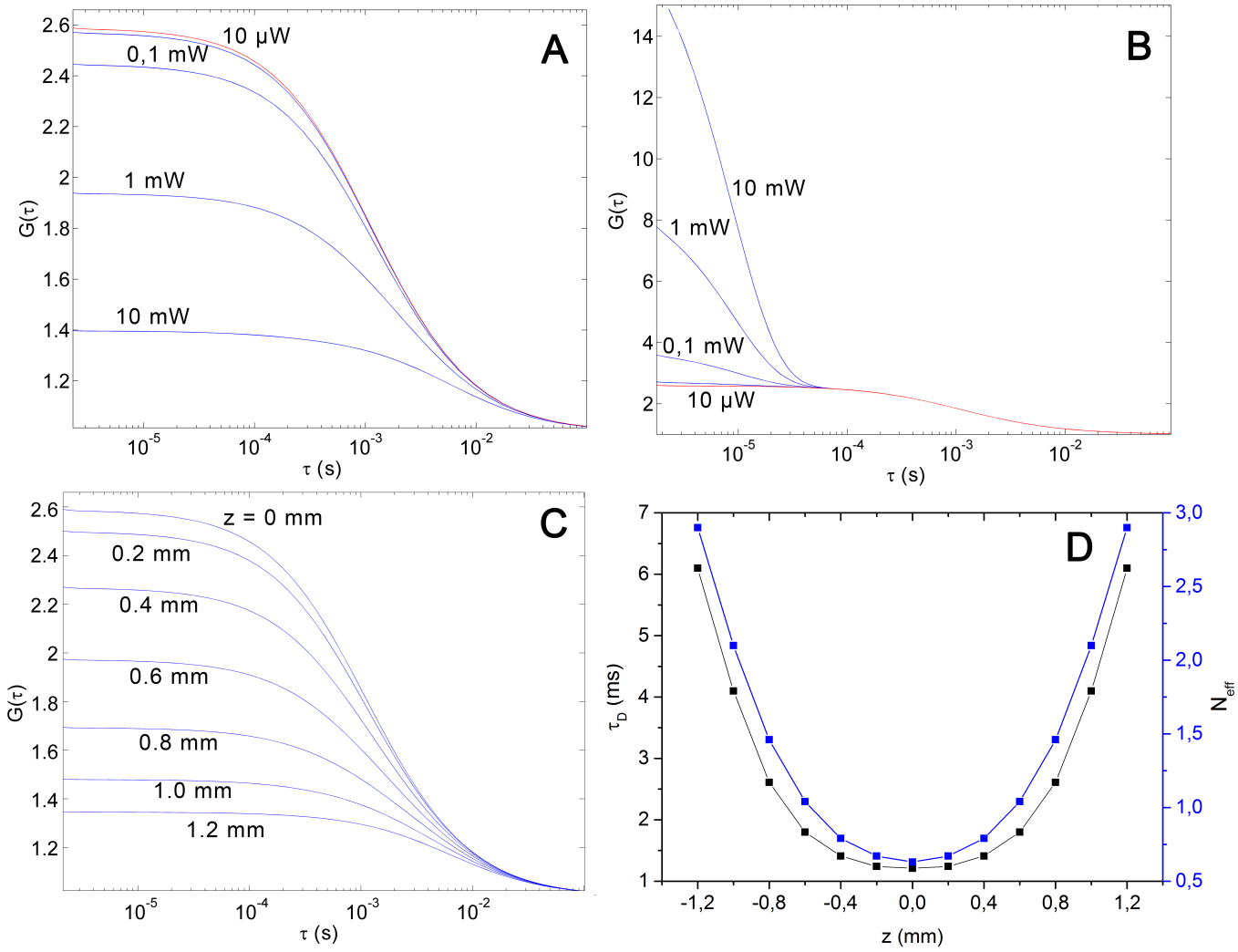

the optical saturation of the fluorophores results in large deviations from the actual model parameters $\tau_D = 1$ ms, and $N_{eff} = 0.63$ (Fig. 5.1A). The impact of axial positioning (z-scan) on τ_D and N_{eff} is quite similar (Fig. 5.1C). Obviously, these parameters increase along with the effective beam radius. Fitting the axially dependent parameters in Eq (5.29) to the parabolic curves of Fig. 5.1D) yield beam waist radiuses of 198 ± 3 nm for N_{eff} and 201 ± 5 nm for τ_D. In addition, it is observed that triplet state fractional population becomes dominant with increasing laser power, as expected (Fig. 5.1B).

Table 5.1: Fitting parameters from the modeled autocorrelation functions with varying laser power. (A) Diffusion time τ_D and effective number of fluorophores N_{eff} under optical saturation (no triplet blinking). (B) Triplet-state lifetime τ_T and average population fraction $\overline{T}$ with no optical saturation.

	A		**B**	
Laser power	τ_D (ms)	N_{eff}	τ_T (µs)	$\overline{T}$
10 µW	1.1	0.64	13	0.08
0.1 mW	1.2	0.69	10	0.43
1 mW	1.9	1.94	9.1	0.80
10 mW	5.2	5.2	8.8	0.91

Finally, one should note that in real experiments the approximative functions of Eqs. 5.28 and 5.30 are fitted to the data, and the beam waist radius w_0 is obtained from the z-scan. Therefore, the previous calculations are not meant to emphasize the applicability of approximations for that utility, but rather to demonstrate the general influence of system parameters on the autocorrelation function.

Chapter 6

Langmuir monolayers

While being one of the nature's most abundant classes of molecules, lipids have many structural and functional roles in living organisms. Cell membranes consist of vast amounts of different lipids and proteins, which due to their amphiphilic structure form bilayers in a water environment. Until the 1990s, the nature of molecular ordering in cell membranes was much under debate. Despite the difficulties in studying nanoscaled structures, it was finally confirmed that cell membranes indeed have *lipid rafts*. These segregated areas, *domains*, exist in a *liquid-ordered* (L_o) phase, stabilized by the cholesterol molecules within them [44]. The rafts have been revealed to participate in important cellular functionalities such as in the transport of cholesterol from the trans-Golgi network to the membrane [45].

Fortunately, there exist many ways to mimic biomembranes in laboratory conditions. For the domains to become visually inspectable, it is of interest to find proper experimental conditions in order to grow the domain size to several micrometers. However, this is way above the actual raft dimensions in biomembranes and does not take into account the fact that the raft may be under cellular regulation [46]. Usually, "rafts" are explored in vesicles, supported bilayers and monolayers. A Langmuir monolayer forms when the lipid molecules are injected into the water–air-interface (Fig. 6.1). A substantial dipole potential arises between the hydrophilic lipid head groups and water molecules while the hydrophobic carboxyl chains point towards the air. One could argue that this kind of model is far from representing a real biomembrane. However, the versatility of Langmuir monolayers ensues from the capability of controlling the lipid composition and *surface pressure* simultaneously along with the presence of subphase-lipid interactions, a task not possible for vesicle systems, for instance. The surface pressure of a monolayer is defined as $\Pi = \gamma - \gamma_0$, where γ_0 stands for surface tension of a pure subphase. Langmuir trough barriers control the pressure, which is measured with a metal probe (see section 7.2 for details). Barriers can increase and decrease the *mean molecular area*, usually denoted as a with units of $Å^2$/molecule. The measurement of surface pressure as a function of the molecular area gives an *isotherm*, $\Pi(a)$.

Depending on the temperature and surface pressure, lipids in the monolayer can express phase behavior. Most lipids, such as POPC, remain in the liquid-expanded (LE) phase, but some lipids experience a transition to the liquid-condensed (LC) phase at higher surface pressures. Phospholipid-cholesterol interactions have important characteristics in Langmuir monolayers by limiting the liquid-expanded nature of the films [47]. A perhaps

Figure 6.1: Schematic of a Langmuir monolayer experiment

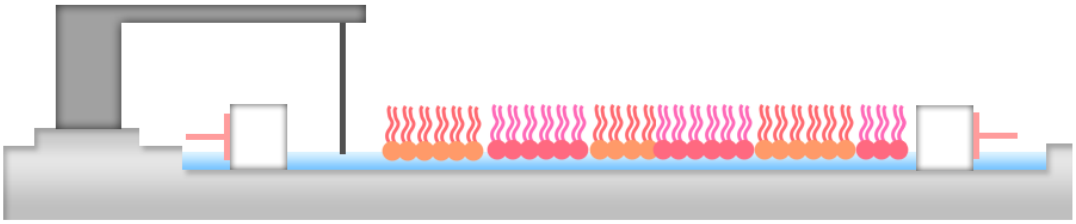

surprising result originally found by epifluorescence methods is that in addition to coexisting phases of the same type of lipids, monolayers can exhibit lipid domains similar to those in biomembranes, consisting of liquid-ordered phase of mainly sphingomyelin and cholesterol. The coexistence of these phases has been traditionally explained in terms of dipole density differences. When the size of the liquid-ordered phase is diminishing, the decrease in free energy due to the dipole-dipole repulsions in this phase competes with increasing energy from the line tension between the coexisting phases [48]. At balance, the free energy function of the system is minimized, which allows to calculate the domain equilibrium size. After a certain surface pressure value is reached, the domains undergo *miscibility transition* and vanish, at least in the resolution limit of optical microscopy. The lack of change in average dipole potential upon this transition suggests that line tension is a major factor contributing to the domain dynamics [15]. Some authors have suggested that line tension is related to the unmatched thickness between the phases, which arises from energetic cost for exposing lipid acyl chains to air at the domain boundaries [49,50].

The free-area model for self-diffusing particles of one molecular species has proven to be useful in single-lipid diffusion studies [51–53]. The model relates diffusion to the available free area $a_f = a - a_0$ in a lateral lipid lattice, where a is the molecular area obtained from Langmuir experiments, and a_0 is the core area of a single lipid (~ 42 Å^2 for a phospholipid). The model is described by the equation

$$\ln \frac{D_T}{D_{max}} = \gamma \frac{a_c}{a_f}, \tag{6.1}$$

where D_{max} represents the maximal diffusion coefficient corresponding to an ideally expanded monolayer, a_c is the critical area per molecule where lateral diffusion becomes possible, and γ is a constant describing the overlapping of free areas ($0.5 < \gamma < 1$) [54]. Given the inverse proportionality between D_T and τ_D (when beam radius w is constant in all transverse planes), the free-area model can be approximated as

$$\ln \frac{\tau_D}{\tau_{min}} = \frac{a_f}{a_c} = \frac{\beta}{a_f}, \tag{6.2}$$

where parameter β can be obtained from the least squares fit.

Part II

Experiments

Chapter 7

Materials and methods

The contents of this chapter have been published in [16].

7.1 Sample preparation

Ternary lipid monolayers consisting of 1-Palmitoyl-2-azelaoyl-*sn*-glycero-3-phosphocholine (POPC), cholesterol (Chol) and porcine brain sphingomyelin (SM) were prepared on the air-aqueous interface (150 mM NaCl subphase) from the chloroform solution with a Hamilton syringe. For oxidation studies, 1-palmitoyl-2-azelaoyl-*sn*-glycero-3-phosphocholine (PazePC) and 1-palmitoyl-2-(9'-oxononanoyl)-*sn*-glycero-3-phosphocholine (PoxnoPC) were also introduced. All the lipids were purchased from Avanti Polar Lipids (Alabaster, AL). Atto488-NSH-ester (Atto-TEC, Siegen, Germany) was covalently reacted with 1-palmitoyl-2-oleoyl-*sn*-glycero-3-phosphoethanolamine (POPE), followed by separation of the free, non-reacted dye from the labeled lipid (POPE-Atto488) using chromatography on silica gel column. Fluorophore to lipid ratios of 1:300 000 and 1: 1 000 were used in FCS and wide-field microscopy (WFM) measurements, respectively.

A rubber spacer was inserted to elevate the cover glass window in the bottom of the Langmuir trough in order to counterbalance the very short (0.28 mm) working distance of the objective. The cover glass was saturated with bovine serum albumin (BSA) to achieve good surface wetting. Water evaporation turned out to be an issue and was avoided by pumping buffer in the trough on the other side of the barrier. The rate of buffer addition was adjusted to match the evaporation during the experiments. In addition, to reduce the surface flow and to maintain constant experimental conditions, a transparent partially-sealed box was used to enclose the trough. The measurement conditions were kept at a constant temperature of 24 °C during all FCS and WFM measurements.

7.2 Measurements

The surface pressure was measured with a Langmuir Teflon trough (μtrough XS, Kibron, Helsinki, Finland). Two symmetrically moving Teflon-barriers controlled the physical trough area by using the dedicated software while surface pressure was monitored by a Ni-chrome wire attached to a microbalance. Unlike for the conventionally employed

Figure 7.1: Confocal microscopy FCS setup built for the experiments.

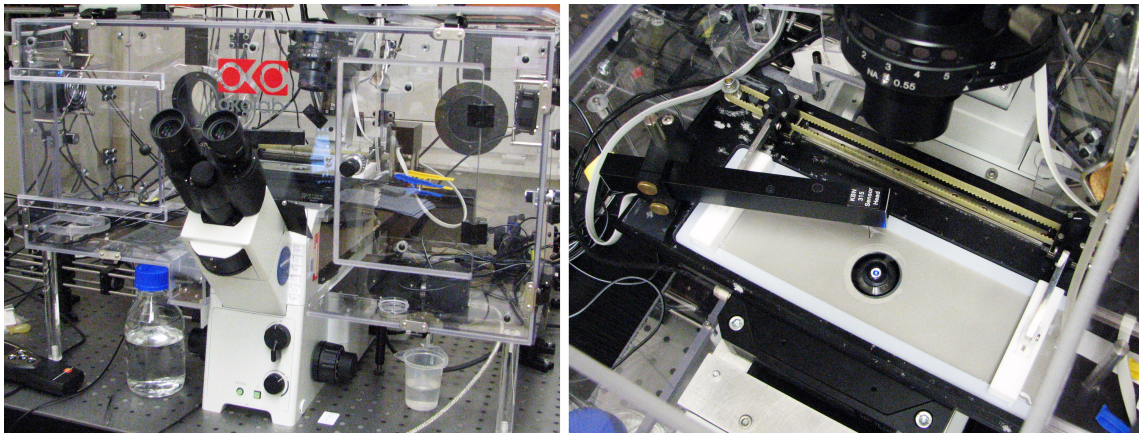

Pt probes, all the contact angles for Ni-chrome are identical, diminishing the artefactual hysteresis between film compression and relaxation [55]. Stable constant-area measurements of surface pressure could not be obtained due to the relatively large pressure-area hysteresis in the compression-expansion isotherms. As POPC has been shown to be more resistant to oxidation-induced surface pressure drop than other unsaturated phospholipids, this is probably not the consequence of the lipid oxidation [56–58]. The hysteresis could indicate both film relaxation due to the abruptly stopped compression and high sensitivity of the metal probe. The latter was also observed during the sensor calibration. However, no significant area loss or reduction in fluorescence signal was detected during the first two compression-expansion cycles.

The FCS measurements were performed on a home-built inverted confocal microscope setup based on Olympus IX 71 (Olympus, Hamburg, Germany) microscope body (Fig. 7.1) . The dye was excited by Picosecond Laser Diode (LDH-P-C-470B; PicoQuant GmbH, Germany) and the excitation laser intensity was controlled by acusto-optical modulator AOM (MT200A0.5-VIS; AA OPTO-ELECTRONIC, Orsay, France). Dichroic mirror (Chroma Technology Corporation, VT, USA) reflected the collimated excitation laser beam, focused into the sample by Olympus water immersion objective (60x magnification, NA 1.2, working distance 0.28 mm). The same objective collected the emitted fluorescence light. After passing through an emission filter (515/50, Omega Optical, VT, USA), the light was detected by SPAD detector (MPD, PicoQuant GmbH, Berlin, Germany). The fluorescence coming from out-of-focus axial planes was cut using a 50 µm pinhole. The laser intensity was kept at 10 µW in order to prevent fluorophore photobleaching and saturation. The axial positioning during z-scan FCS was controlled by the piezo system (PI P-562, Karls-ruhe, Germany). The fluorescence intensity fluctuations were correlated and analyzed using Origin software.

Fluorescence time traces were obtained during Langmuir film compression. In most of the intensity time traces a surface flow of the whole system was observed, which results in a sudden decrement in fluorescence signal because of the presence of non-fluorescent structures in the detection volume. The time scales of the domains wandering through the

focus due to the surface flow were found to be a three orders of magnitude slower (1-2 s) than the lateral diffusion of fluorescent lipids (~ ms). The separation of time scales made it possible to analyze intensity time traces using autocorrelation analysis (two-component model, Eq. (5.24)) despite the sudden decreases in the fluorescence signal. For Atto-488, the contribution of the triplet blinking to the amplitude is very low (less than 5 %). Still, triplet parameters were initially included in the analysis of the data.

In order to reach correct diffusion times with monolayer being exactly in the beam waist minimum of the detection volume, positional scanning along the optical axis was achieved using z-scan with step-size of 200 nm [59]. During the compression process, multiple z-scans were implemented while continuously measuring surface pressure. Each z-scan consisted of several FCS traces (10 s each) which were recorded in stepwise manner. Subphase position was checked and adjusted between each scan. Autocorrelation analysis was performed assuming the Lorentzian-Gaussian profile of the laser beam (Eqs. 5.30 and 5.29).

The imaging was performed on a home-built inverted wide-field microscope (WFM), with same microscope body as used for FCS. Continuous excitation (Coherent, Saphire 488-150CW, CA, USA) modulated by acousto-optical tunable filter (AOTFnC-400.650-TN, AA OPTO-ELECTRONIC, Orsay, France). The sample was illuminated by water immersion objective (Olympus, 60×, NA 1.2, working distance 0.28 mm) and the same objective was used for the collection of emitted light. CCD camera (Andor, Belfast, UK) detected the emitted photons that passed through the emission filter (515/50, Omega Optical, VT, USA) . The used pixel size was 167 nm, frame rate 1/30 ms. During the experiments, the laser intensity was varied to get best imaging contrast and to prevent the saturation of camera. The images were processed using ImageJ and Origin software.

Chapter 8

Results

The contents of this chapter have been published in [16].

8.1 Oxidized phospholipids in POPC monolayers

First, a binary mixture of POPC and PazePC with an oxidatively truncated acyl chain with a terminal carboxylic acid moiety in *sn*-2 position of the backbone glycerol was used. A comparison of POPC films with those additionally containing 25 mol-% of PazePC did not reveal any obvious changes in the slope of the linear dependence of diffusion time versus surface pressure (Fig. 8.1A). Instead, the differences become evident when the logarithm of τ_D is plotted against the reciprocal value of free area a_f (Fig. 8.1B), which is in accordance with the free area model. The kink at $a_f^{-1} \approx 0.022$ Å^{-2} suggests that the model seems to fail for dilute films ($a > 87$ Å^2), as observed previously [60]. When the linear fits of molecular area versus $1/\tau_D$ (Fig. 8.1C) are extrapolated to infinitely long diffusion times (i.e. no diffusion), the critical areas for those compositions can be estimated. The values of ~ 46 Å^2 and ~ 50 Å^2 for pure POPC and POPC/PazePC mixtures indicate slight area expansion for the latter film. Values for different parameters are summarized in Table 8.1. Higher β-values indicate that when the free area decreases, the diffusion time will increase more rapidly in POPC/PazePC. Overlapping-factor γ was estimated by dividing the value of β obtained from the free-area model by the extrapolated critical molecular area a_c.

8.2 Oxidized phospholipids in a ternary "raft mixture"

Lipid monolayers with coexisting liquid-ordered/disordered (L_o/L_d) phases were examined under the influence of oxidized phospholipids. POPC/SM/Chol mixtures in the molar ratio of 1.5/1.5/1 were chosen in order to mimic lipid compositions in mammalian cell membranes and also for the possibility to follow micrometer-size lipid domains by optical microscopy. For samples containing oxidatively modified PCs, 12.5 % or 25 % of POPC fraction (i.e. 4.7 or 9.4 mol-% of the overall lipid mixture) was substituted by PazePC or PoxnoPC, respectively. The monolayer was stained with POPE-Atto488 and there was no

Figure 8.1: Diffusion time measurements for POPC/PazePC films at 24 °C with 0 % (■) and 25 % (○) of PazePC. (A) Diffusion time τ_D vs. surface pressure Π. (B) $\ln \tau_D$ vs. inverse of free area a_f. (C) Inverse of τ_D vs. molecular area A.

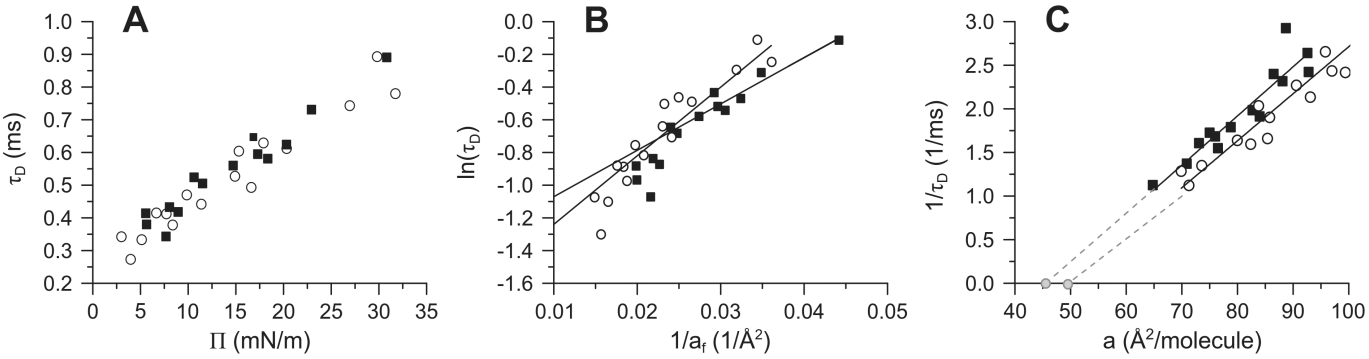

significant partitioning of fluorophores into the liquid ordered phase in both confocal and wide-field microscopy.

WFM imaging provided information on the morphology of the L_o-domain structures upon compression and subsequent expansion (Fig. 8.2). The experiments were performed for lipid mixture with no oxPL and for mixtures with 9.4 mol-% of PazePC or PoxnoPC. During early stages of monolayer compression, domains preserve their circular shape until the onset of the miscibility transition (at 12 mN/m for the film without oxPLs, 15 mN/m and 18 mN/m for films with 9.4 mol-% PazePC and PoxnoPC, respectively). Thus, the domains remain unaffected by the compression, reducing the free area for phospholipid molecules to diffuse in the L_d-phase. Higher miscibility transition pressure values for oxPL-containing lipid films confirm the previously shown stabilization of phase separation in lipid monolayers by oxPLs [15]. The diffusion in the L_o-phase was not measured.

The size of domains is slightly smaller for oxPL-containing films (domain size distribution are 2.12 ± 0.61 μm, 1.91 ± 0.39 μm and 2.05 ± 0.48 μm for oxPL-free, PazePC and PoxnoPC monolayers, respectively), which could indicate oxidation-induced increase in line tension, the main factor contributing to the domain stability [61]. When miscibility transition pressure is exceeded, the domains lose their integrity and the labeled lipids can

Table 8.1: Free-area model parameters obtained from Fig. 8.1B. Value of γ is estimated by dividing the value of β with extrapolated critical area from Fig. 8.1C.

	POPC	POPC/PazePC (75:25)
β	28 ± 2.9	42 ± 5.8
τ_{min} (ms)	0.19 ± 0.05	0.17 ± 0.06
a_c (Å^2)	46	50
γ	0.61	0.84

enter them, evident as loss of domain structure. The reformation of domains during the monolayer expansion could indicate relative system stability for lipid films free of oxPLs and those with PazePC. Surprisingly, expansion of PoxnoPC containing samples results in a highly inhomogeneous system in terms of domain morphology. While there were no differences in miscibility transition pressures for compression and expansion in PazePC films, a slight transition pressure drop was detected in films with no oxPL and also with PoxnoPC.

Continuous compression while obtaining FCS data revealed distinct sigmoidal diffusion behavior as the surface pressure increases (Fig. 8.3A). The upper and lower limits in diffusion time can be found from the Boltzmann fits of the data. Diffusion times reach the maximum value of $\tau_D \sim 1.5$ ms for samples with and without oxPLs. Similarly, the minimal diffusion time of 0.29 ms was found in low surface pressures regardless of the L_d-phase composition. As expected, zero values of the second derivatives of the corresponding Boltzmann fits (i.e. the pressures yielding maximal diffusion slowdown) are close to the miscibility transition pressures found in wide field microscopy (Fig. 8.3B). Boltzmann fits give the value of 11.7 mN/m for films without oxPLs (12 mN/m in WFM) and 18.7 mN/m and 20.4 mN/m for 9.4 mol-% PazePC (15 mN/m in WFM) and PoxnoPC

Figure 8.2: WFM imaging of monolayer compression and expansion cycles at 24 °C. Panel A) corresponds to POPC/SM/Chol (1.5/1.5/1 molar ratio), panel B) and panel C) show monolayers where 25 % of POPC fraction is substituted by 9.4 mol-% PazePC (panel B) or 9.4 mol-% PoxnoPC (panel C). Notably, the completely expanded monolayer in lipid samples containing PoxnoPC is highly heterogeneous.

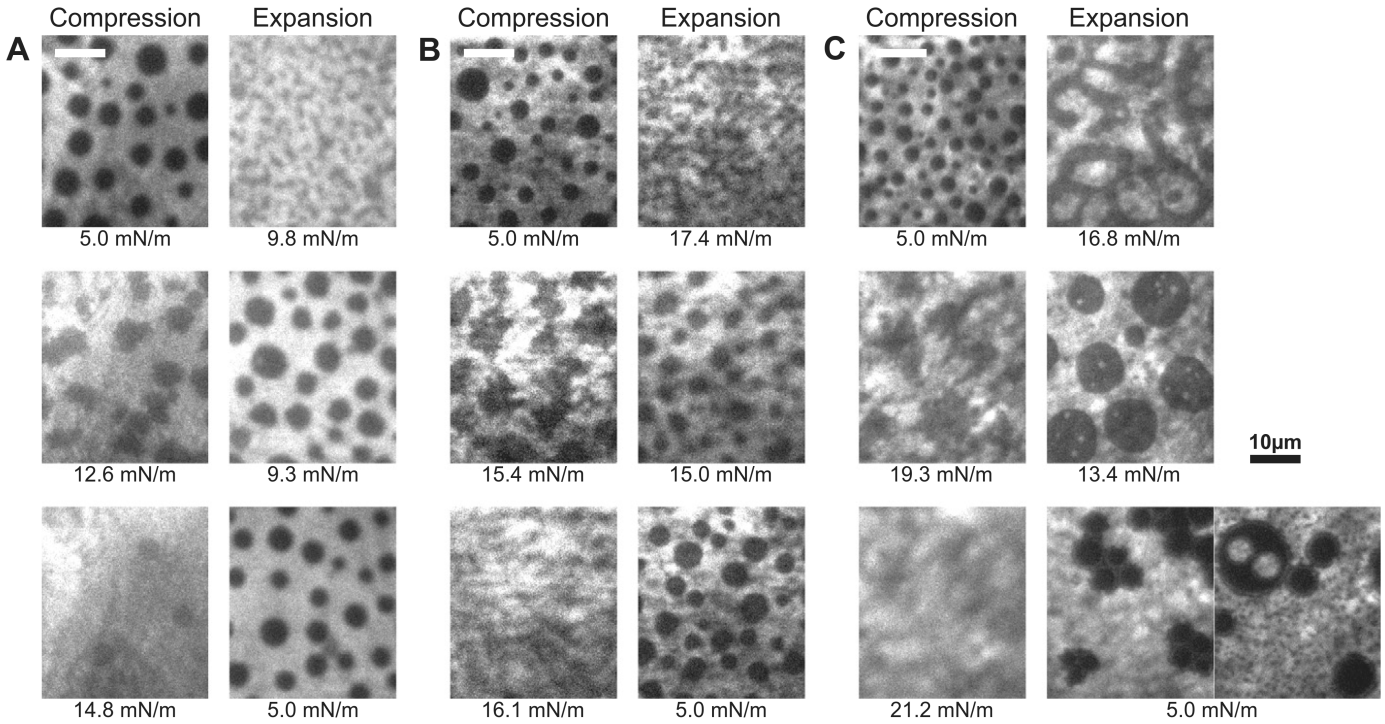

Figure 8.3: (A) Diffusion time τ_D vs. surface pressure Π and (B) second derivative of $\tau_D(\Pi)$ for (POPC + PazePC/PoxnoPC)/pSM/Chol (1.5/1.5/1 molar ratio) mixtures at 25 °C. Amount of PazePC was set as 0 % (■), 12.5 % (△) and 25 % (●) of the phospholipid fraction. Data for PoxnoPC (25 % of the PL fraction, ◇) is provided for comparison. Corresponding Boltzmann fits are included. Dotted line indicates the data fit for pure POPC film.

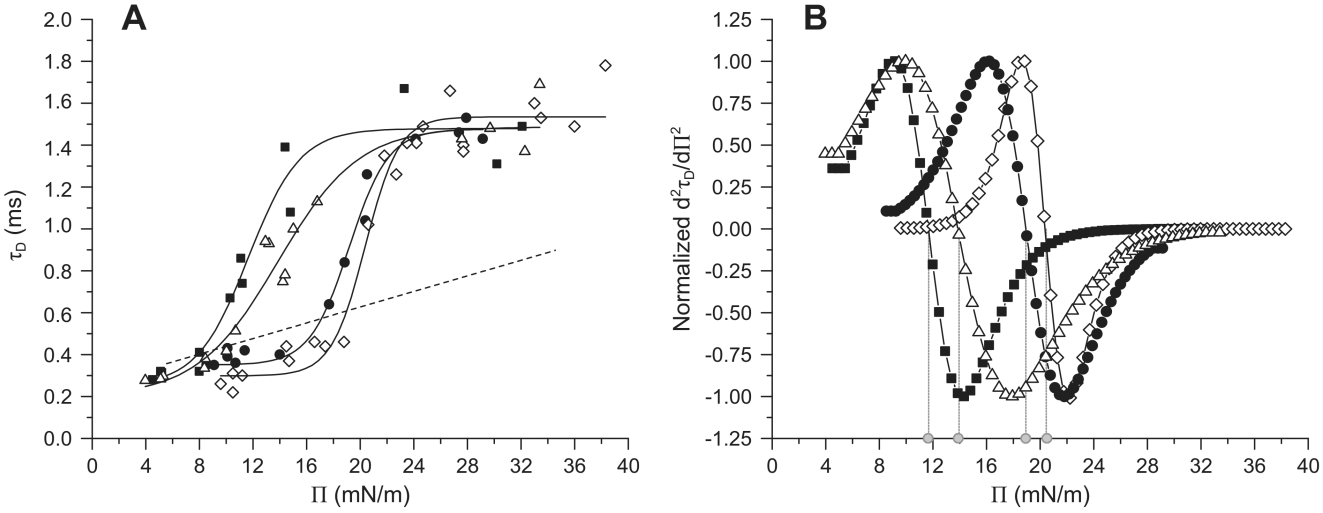

(18 mN/m in WFM), respectively. Thus, a quantitative prediction of miscibility transition pressures can be obtained from the diffusion time measurements. For both systems containing oxPLs the quantitative values determined by FCS are slightly higher than those observed in WFM. However, in the case of WFM, the determination of phase transition pressure relies on subjective visual observation.

When comparing the two oxPLs, the aldehyde derivative seems to be more efficient in stabilizing the phase separation. As suggested by Khandelia and Mouritsen, the azelaoyl chain in PazePC would loop out from the hydrophobic core, with its preferential angle of orientation being 160 degrees with respect to the membrane normal [62]. On the other hand, the oxo-nonaoyl chain of PoxnoPC shows an angle distribution of approximately 80 degrees, perpendicular to the membrane normal. Since choline in sphingomyelin is supposed to be oriented towards the membrane, there could be a hypothetical interaction between the oxygen in the truncated acyl chains of oxPLs and the nitrogen of choline moiety of sphingomyelin [63]. The orientational difference in acyl chains of oxPLs could result in a tighter interaction of PoxnoPC and sphingomyelin and thus better stabilization of lipid structures. Also, the possible association of the sodium counterions from the subphase with PazePC carboxylic acid (COO-) moiety could make any interactions with the domain boundaries less probable.

Along with the possible interactions at the domain boundary, thickness mismatch has been widely accepted as an explanation for domain separation and stabilization (Chap. 6). Considering that the average angular orientations of oxPL acyl chains are directed away

from the hydrocarbon-air interface, the structural order in the L_d-phase chain region could be compromised in higher surface pressures. This would indeed induce larger thickness mismatch between L_o- and L_d-phases. Anyhow, it is unclear whether the seemingly better stabilization properties of PoxnoPC compared to PazePC are due to increased height mismatch or possible tighter interactions with other membrane constituents.

Exponentially increasing diffusion times upon approaching the miscibility transition suggests that this transition is a continuous nonlinear event. Condensation effect would finally lead to the lack of sufficient thickness mismatch between the phases and eventually result in domain disintegration. Judging from series of images obtained from WFM near the phase transition, an insignificant fraction of merging domains was observed, suggesting that phase mixing is not due to the domain merging. Instead, domains seem to merge randomly whenever coming sufficiently close. According to Akimov *et al.*, this would mean separation distances of only 1-2 nm [49]. Based on the WFM images, no significant differences in domain sizes for different L_d-phase compositions was calculated, which is in contradiction with the notion that increasing line tension should promote larger domains [61].

Chapter 9

Summary and conclusions

In the first part of the thesis, the theory of fluorescence correlation spectroscopy was reviewed. In Chap. 2, it was argued that in the limit of high numerical apertures (intense beam focusing) and substantial beam over-filling ($f_0 \gg 1$), formulas developed using diffraction theory differ from the fundamental Gaussian laser beams in two distinctive ways. First, the shape and width in both radial and axial directions become dissimilar. Second, a considerable amount of beam energy is carried by the diffraction fringes of non-Gaussian beams. While the former can be compensated via the curve fitting procedure of autocorrelation analysis, the latter cannot. Since the requirement for a small detection volume averts the possibility to reduce the beam focusing and the filling factor of the objective aperture, the more rigorous formulas cannot be explicitly approximated by a Gaussian.

The laser light has the capability to excite and re-excite a particular class of molecules permitting the HOMO-LUMO transitions, which is the essence of fluorescence phenomenon. Chapter 3 demonstrated how the absorption rate of a molecule depends both on the intensity of the excitation light source and the orientation of the molecular transition dipole moment at the time of excitation. Then the rate analysis of simple chemical kinetics was applied to determine the rate of fluorescence emission under constant illumination. It was concluded that the fluorescence emission rate cannot be infinitely increased due to the optical saturation. Chapter 4 described how a fluorophore located at some point of sample space emits radiation, again dependent on the current transition dipole moment orientation. An epifluorescence configuration first images the dipolar emission field and then the dipole PSF is spatially convolved with a circular pinhole. The resulting point spread function describes the efficiency of the confocal system to detect photons from the sample space.

Chapter 5 treated the FCS autocorrelation analysis with particular formalism, taking into account the stochastic nature of various processes affecting the detected signal. Due to the mathematical complexity of both the excitation laser beam profile and detector point spread function, the molecular detection function has to be approximated by a Gaussian-Lorentzian function in order to solve the autocorrelation function analytically. In its most basic form, autocorrelation function has only two parameters, average diffusion time (τ_D) and effective number of molecules in the focus (N_{eff}). Additionally, triplet state blinking can be incorporated if the triplet state lifetime (τ_T) and steady state population fraction

$\overline{T}$ are replaced with their spatial averages. Additionally, triplet state blinking may be incorporated if the triplet state lifetime and steady state population fraction are spatially averaged. Z-scan was presented as a method to determine beam waist radius w_0 without additional calibration of the system using a fluorophore with known diffusion properties.

In the experimental part, the effect of oxidatively truncated phosphatidylcholines on the lipid diffusion was described and quantified in ternary lipid films using the home built FCS instrumentation. The fluorescence intensity time traces from the probed lipids were collected while continuously compressing or expanding the monolayer. The experiments consisted of multiple z-scans where the positioning of the laser beam was axially varied. The reviewed theory in Part I provided with the appropriate fitting functions to retrieve the characteristic times for a lipid to diffuse laterally through the laser focus. First, the diffusion times were obtained by fitting the analytic two-component model to the experimental autocorrelation functions. Then, the diffusion times belonging to the individual z-scans were plotted against the axial laser position, allowing to determine the minimum diffusion times of the scans. Thus, all the presented diffusion time parameters were obtained from the parabolic minima corresponding to the positions where the monolayer coincided with the laser beam waist.

In Chap. 8, it was first shown that PazePC in a POPC monolayer increases the lipid area by about 4 $Å^2$ in comparison to pure POPC films. Then the ternary "raft mixtures" and the impact of PazePC and PoxnoPC on L_o-structures were studied. Visualization using WFM did show no significant differences in the domain morphology for oxPL-free and PazePC containing monolayers. On the other hand, lipid films with PoxnoPC had peculiar inhomogeneities upon both compression and expansion. The surface pressure needed for the L_d–L_o miscibility transition increased in the sequence oxPL-free-PazePC-PoxnoPC. Miscibility transition pressures were measured as 11.7 mN/m for films with no oxPL, 18.7 mN/m for 9.4 mol-% PazePC, and 20.4 mN/m for 9.4 mol-% PoxnoPC containing lipid films. In conclusion, it was confirmed by both FCS and WFM methods that oxPLs prevent the miscibility transition of the lipid "raft" domains in Langmuir monolayers.

References

[1] D. Magde, E. Elson, and W. W. Webb, "Thermodynamic fluctuations in a reacting system - measurement by fluorescence correlation spectroscopy," *Physical Review Letters*, vol. 29, no. 11, p. 705, 1972.

[2] B. J. Berne and R. Pecora, "Light scattering as a probe of fast reaction kinetics: The depolarized spectrum of Rayleigh scattered light from a chemically reacting medium," *The Journal of chemical physics*, vol. 50, no. 2, pp. 783–791, 1969.

[3] S. R. Aragón and R. Pecora, "Fluorescence correlation spectroscopy and Brownian rotational diffusion," *Biopolymers*, vol. 14, no. 1, pp. 119–137, 1975.

[4] S. R. Aragón and R. Pecora, "Fluorescence correlation spectroscopy as a probe of molecular dynamics," *The Journal of chemical physics*, vol. 64, no. 4, pp. 1791–1803, 1976.

[5] G. Vámosi, N. Baudendistel, C.-W. V. der Lieth, N. Szalóki, G. Mocsár, G. Müller, P. Brázda, W. Waldeck, S. Damjanovich, and J. Langowski, "Conformation of the c-Fos/c-Jun complex in vivo: A combined FRET, FCCS, and MD-modeling study," *Biophysical journal*, vol. 94, no. 7, pp. 2859–2868, 2008.

[6] T. Dertinger, V. Pacheco, I. von der Hocht, R. Hartmann, I. Gregor, and J. Enderlein, "Two-focus fluorescence correlation spectroscopy: A new tool for accurate and absolute diffusion measurements," *ChemPhysChem*, vol. 8, no. 3, pp. 433–443, 2007.

[7] Z. K. Gryczynski, "FCS imaging – a way to look at cellular processes," *Biophysical journal*, vol. 94, no. 6, pp. 1943–1944, 2008.

[8] H.-T. He and D. Marguet, "Detecting nanodomains in living cell membrane by fluorescence correlation spectroscopy," *Annual Review of Physical Chemistry*, vol. 62, pp. 417–436, 2011.

[9] P. Schwille and E. Haustein, "Fluorescence correlation spectroscopy – an introduction to its concepts and applications," 2001.

[10] R. Rigler and E. S. Elson, Eds., *Fluorescence Correlation Spectroscopy: Theory and Applications*, ser. Springer Series in Chemical Physics. Springer Berlin Heidelberg, 2001.

[11] P. K. Kinnunen, K. Kaarniranta, and A. K. Mahalka, "Protein-oxidized phospholipid interactions in cellular signaling for cell death: From biophysics to clinical correlations," *Biochimica et Biophysica Acta (BBA)-Biomembranes*, vol. 1818, no. 10, pp. 2446–2455, 2012.

[12] R. Volinsky and P. K. J. Kinnunen, "Oxidized phosphatidylcholines in membrane level cellular signaling from biophysics to physiology and molecular pathology," *FEBS Journal*, vol. 280, no. 12, pp. 2806–2816, 2013.

[13] S. Orrenius, V. Gogvadze, and B. Zhivotovsky, "Mitochondrial oxidative stress: Implications for cell death," *Annual Review of Pharmacology and Toxicology*, vol. 47, no. 1, pp. 143–183, 02/01; 2013/01 2007.

[14] R. Volinsky, L. Cwiklik, P. Jurkiewicz, M. Hof, P. Jungwirth, and P. K. Kinnunen, "Oxidized phosphatidylcholines facilitate phospholipid flip-flop in liposomes," *Biophysical journal*, vol. 101, no. 6, pp. 1376–1384, 2011.

[15] R. Volinsky, R. Paananen, and P. K. J. Kinnunen, "Oxidized phosphatidylcholines promote phase separation of cholesterol-sphingomyelin domains," *Biophysical journal*, vol. 103, no. 2, pp. 247–254, 7/18 2012.

[16] P. Parkkila, M. Štefl, A. Olżyńska, M. Hof, and P. K. Kinnunen, "Phospholipid lateral diffusion in phosphatidylcholine-sphingomyelin-cholesterol monolayers; effects of oxidatively truncated phosphatidylcholines," *Biochimica et Biophysica Acta (BBA)-Biomembranes*, vol. 1848, no. 1, pp. 167–173, 2015.

[17] L. Novotny and B. Hecht, *Principles of Nano-Optics*. Cambridge University Press, 2006. [Online]. Available: http://dx.doi.org/10.1017/CBO9780511813535

[18] E. Wolf, "Electromagnetic diffraction in optical systems. I. an integral representation of the image field," *Proceedings of the Royal Society of London.Series A, Mathematical and Physical Sciences*, pp. 349–357, 1959.

[19] B. Richards and E. Wolf, "Electromagnetic diffraction in optical systems. II. structure of the image field in an aplanatic system," *Proceedings of the Royal Society of London.Series A.Mathematical and Physical Sciences*, vol. 253, no. 1274, pp. 358–379, 1959.

[20] R. H. Webb, "Confocal optical microscopy," *Reports on Progress in Physics*, vol. 59, no. 3, p. 427, 1996.

[21] E. S. Bahaa and C. T. Malvin, *Beam Optics*, ser. Fundamentals of photonics. Wiley InterScience Publications, 1991, ch. 3, p. 86.

[22] L. M. Davis and G. Shen, "Accounting for triplet and saturation effects in FCS measurements," *Current Pharmaceutical Biotechnology*, vol. 7, no. 4, pp. 287–301, 2006.

[23] J. R. Lakowicz, *Topics in Fluorescence Spectroscopy: Volume 4: Probe Design and Chemical Sensing*. Springer Science & Business Media, 1994, p. 301.

[24] S. Kou, X. S. Xie, and J. S. Liu, "Markov Chain Monte Carlo in the analysis of single-molecule experimental data," *Energy*, vol. 21, p. k12, 2003.

[25] A. Papoulis and S. U. Pillai, *Probability, Random Variables, and Stochastic Processes*, 3rd ed. Tata McGraw-Hill, 2002.

[26] J. Widengren, U. Mets, and R. Rigler, "Fluorescence correlation spectroscopy of triplet states in solution: a theoretical and experimental study," *The Journal of physical chemistry*, vol. 99, no. 36, pp. 13 368–13 379, 1995.

[27] Ülo Mets, J. Widengren, and R. Rigler, "Application of the antibunching in dye fluorescence: measuring the excitation rates in solution," *Chemical Physics*, vol. 218, no. 1, pp. 191–198, 1997.

[28] H. Arnoldus and G. Nienhuis, "Photon statistics of fluorescence radiation," *Journal of Modern Optics*, vol. 33, no. 6, pp. 691–702, 1986.

[29] I. Gregor, D. Patra, and J. Enderlein, "Optical saturation in fluorescence correlation spectroscopy under continuous-wave and pulsed excitation," *ChemPhysChem*, vol. 6, no. 1, pp. 164–170, 2005.

[30] J. Enderlein, "Fluorescence correlation spectroscopy (IUPAC technical report)," *Pure and Applied Chemistry*, vol. 85, no. 5, pp. 999–1016, 2013.

[31] L. Arnold and M. Theodosopulu, "Deterministic limit of the stochastic model of chemical reactions with diffusion," *Advances in Applied Probability*, pp. 367–379, 1980.

[32] D. T. Gillespie, "Deterministic limit of stochastic chemical kinetics," *The Journal of Physical Chemistry B*, vol. 113, no. 6, pp. 1640–1644, 2009.

[33] X. Brokmann, J.-P. Hermier, G. Messin, P. Desbiolles, J.-P. Bouchaud, and M. Dahan, "Statistical aging and nonergodicity in the fluorescence of single nanocrystals," *Physical Review Letters*, vol. 90, no. 12, p. 120601, 2003.

[34] J. Enderlein, I. Gregor, D. Patra, T. Dertinger, and U. B. Kaupp, "Performance of fluorescence correlation spectroscopy for measuring diffusion and concentration," *ChemPhysChem*, vol. 6, no. 11, pp. 2324–2336, 2005.

[35] A. Honigmann, C. Walter, F. Erdmann, C. Eggeling, and R. Wagner, "Characterization of horizontal lipid bilayers as a model system to study lipid phase separation," *Biophysical journal*, vol. 98, no. 12, pp. 2886–2894, 2010.

[36] K. K. Jr, A. Ikegami, and S. Kawato, "On the wobbling-in-cone analysis of fluorescence anisotropy decay," *Biophysical journal*, vol. 37, no. 2, pp. 461–464, Feb 1982, lR: 20130924; JID: 0370626; OID: NLM: PMC1328828; ppublish.

[37] A. Szabo, “Theory of polarized fluorescent emission in uniaxial liquid crystals,” *The Journal of chemical physics*, vol. 72, no. 8, pp. 4620–4626, 1980.

[38] P. Kask, P. Piksarv, M. Pooga, U. Mets, and E. Lippmaa, “Separation of the rotational contribution in fluorescence correlation experiments,” *Biophysical journal*, vol. 55, no. 2, pp. 213–220, Feb 1989.

[39] S. M. Sorscher and M. P. Klein, “Profile of a focussed collimated laser beam near the focal minimum characterized by fluorescence correlation spectroscopy,” *Review of Scientific Instruments*, vol. 51, no. 1, pp. 98–102, 1980.

[40] K. Haßler, “Single molecule detection and fluorescence correlation spectroscopy on surfaces,” 2006.

[41] O. Krichevsky and G. Bonnet, “Fluorescence correlation spectroscopy: the technique and its applications,” *Reports on Progress in Physics*, vol. 65, no. 2, 2002.

[42] R. Macháň and M. Hof, “Lipid diffusion in planar membranes investigated by fluorescence correlation spectroscopy,” *Biochimica et Biophysica Acta (BBA) - Biomembranes*, vol. 1798, no. 7, pp. 1377–1391, 7 2010.

[43] S. T. Hess and W. W. Webb, “Focal volume optics and experimental artifacts in confocal fluorescence correlation spectroscopy,” *Biophysical journal*, vol. 83, no. 4, pp. 2300–2317, 2002.

[44] S. Sonnino and A. Prinetti, “Membrane domains and the "lipid raft" concept,” *Current medicinal chemistry*, vol. 20, no. 1, pp. 4–21, 2013.

[45] K. Simons and E. Ikonen, “Functional rafts in cell membranes,” *Nature*, vol. 387, no. 6633, pp. 569–572, 1997.

[46] C. Dietrich, L. Bagatolli, Z. Volovyk, N. Thompson, M. Levi, K. Jacobson, and E. Gratton, “Lipid rafts reconstituted in model membranes,” *Biophysical journal*, vol. 80, no. 3, pp. 1417–1428, 2001.

[47] R. Demel, L. V. Deenen, and B. Pethica, “Monolayer interactions of phospholipids and cholesterol,” *Biochimica et Biophysica Acta (BBA)-Biomembranes*, vol. 135, no. 1, pp. 11–19, 1967.

[48] H. M. McConnell, “Structures and transitions in lipid monolayers at the air-water interface,” *Annual Review of Physical Chemistry*, vol. 42, no. 1, pp. 171–195, 1991.

[49] S. A. Akimov, P. I. Kuzmin, J. Zimmerberg, F. S. Cohen, and Y. A. Chizmadzhev, “An elastic theory for line tension at a boundary separating two lipid monolayer regions of different thickness,” *Journal of Electroanalytical Chemistry*, vol. 564, no. 0, pp. 13–18, 3/15 2004.

[50] J. M. Holopainen, A. J. Metso, J.-P. Mattila, A. Jutila, and P. K. Kinnunen, “Evidence for the lack of a specific interaction between cholesterol and sphingomyelin,” *Biophysical journal*, vol. 86, no. 3, pp. 1510–1520, 2004.

[51] P. F. F. Almeida, W. L. C. Vaz, and T. E. Thompson, "Lateral diffusion in the liquid phases of dimyristoylphosphatidylcholine/cholesterol lipid bilayers: a free volume analysis," *Biochemistry*, vol. 31, no. 29, pp. 6739–6747, 1992.

[52] K. Tanaka, P. A. Manning, V. K. Lau, and H. Yu, "Lipid lateral diffusion in dilauroylphosphatidylcholine/cholesterol mixed monolayers at the air/water interface," *Langmuir*, vol. 15, no. 2, pp. 600–606, 1999.

[53] W. L. Vaz, R. M. Clegg, and D. Hallmann, "Translational diffusion of lipids in liquid crystalline phase phosphatidylcholine multibilayers. a comparison of experiment with theory," *Biochemistry*, vol. 24, no. 3, pp. 781–786, 1985.

[54] H. Möhwald, *Handbook of Biological Physics: Phospholipid Monolayers*. Elsevier Science B.V., 1995, p. 161.

[55] W. E. Momsen, J. M. Smaby, and H. L. Brockman, "The suitability of nichrome for measurement of gas-liquid interfacial tension by the wilhelmy method," *Journal of colloid and interface science*, vol. 135, no. 2, pp. 547–552, 1990.

[56] R. F. Jacob and R. P. Mason, "Lipid peroxidation induces cholesterol domain formation in model membranes," *Journal of Biological Chemistry*, vol. 280, no. 47, pp. 39 380–39 387, 2005.

[57] C. Lai, S. Yang, and B. Finlayson-Pitts, "Interactions of monolayers of unsaturated phosphocholines with ozone at the air-water interface," *Langmuir*, vol. 10, no. 12, pp. 4637–4644, 1994.

[58] J. F. Liljeblad, V. Bulone, E. Tyrode, M. W. Rutland, and C. M. Johnson, "Phospholipid monolayers probed by vibrational sum frequency spectroscopy: instability of unsaturated phospholipids," *Biophysical journal*, vol. 98, no. 10, pp. L50–L52, 2010.

[59] A. Benda, M. Beneš, V. Marecek, A. Lhotský, W. T. Hermens, and M. Hof, "How to determine diffusion coefficients in planar phospholipid systems by confocal fluorescence correlation spectroscopy," *Langmuir*, vol. 19, no. 10, pp. 4120–4126, 2003.

[60] M. Gudmand, M. Fidorra, T. Bjørnholm, and T. Heimburg, "Diffusion and partitioning of fluorescent lipid probes in phospholipid monolayers," *Biophysical journal*, vol. 96, no. 11, pp. 4598–4609, 6/3 2009.

[61] D. W. Lee, Y. Min, P. Dhar, A. Ramachandran, J. N. Israelachvili, and J. A. Zasadzinski, "Relating domain size distribution to line tension and molecular dipole density in model cytoplasmic myelin lipid monolayers," *Proceedings of the National Academy of Sciences*, vol. 108, no. 23, pp. 9425–9430, 2011.

[62] H. Khandelia and O. G. Mouritsen, "Lipid gymnastics: evidence of complete acyl chain reversal in oxidized phospholipids from molecular simulations," *Biophysical journal*, vol. 96, no. 7, pp. 2734–2743, 2009.

[63] J. Aittoniemi, P. S. Niemelä, M. T. Hyvönen, M. Karttunen, and I. Vattulainen, "Insight into the putative specific interactions between cholesterol, sphingomyelin, and palmitoyl-oleoyl phosphatidylcholine," *Biophysical journal*, vol. 92, no. 4, pp. 1125–1137, 2007.